

Which Ion Dominates Temperature and Pressure Response of Halide Perovskites and Elpasolites?

Loreta A. Muscarella,^{1#*} Huygen J. Jöbsis,^{1#} Bettina Baumgartner,¹ P. Tim Prins,¹ D. Nicolette Maaskant,¹ Andrei V. Petukhov,² Dmitry Chernyshov,³ Charles J. McMonagle,³ and Eline M. Hutter^{1*}

1. Inorganic Chemistry and Catalysis group, Debye Institute for Nanomaterials Science and Institute for Sustainable and Circular Chemistry, Department of Chemistry, Utrecht University, Princetonlaan 8, 3584 CB Utrecht, the Netherlands
2. Physical and Colloid Chemistry, Debye Institute for Nanomaterials Science, Department of Chemistry, Utrecht University, Padualaan 8, 3584 CH Utrecht, the Netherlands
3. Swiss–Norwegian Beamlines, European Synchrotron Radiation Facility, 71 Avenue des Martyrs, 38000 Grenoble, France

These authors contributed equally

* Correspondence should be addressed to E.M.Hutter@uu.nl and loretaangela.muscarella@gmail.com

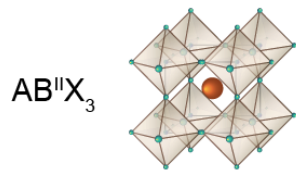
Abstract

Halide perovskite and elpasolite semiconductors are extensively studied for optoelectronic applications due to their excellent performance together with significant chemical and structural flexibility.

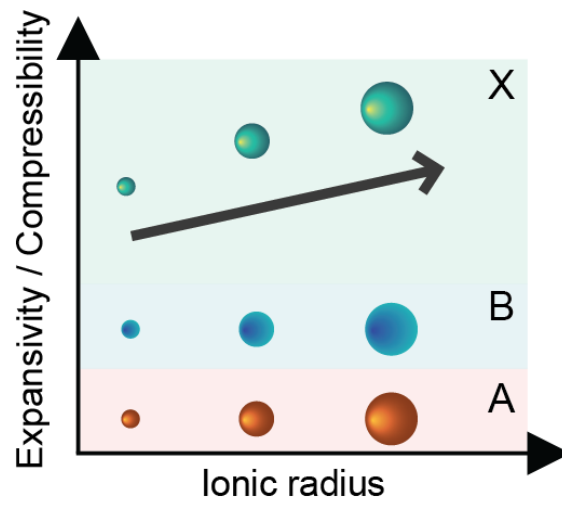
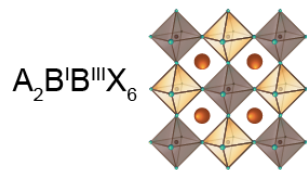
However, there is still limited understanding of their basic elastic properties and how they vary with composition and temperature, which is relevant for synthesis and device operation. To address this, we performed temperature- and pressure-dependent synchrotron-based powder X-ray diffraction (XRD). In contrast to previous pressure-dependent XRD studies, our relatively low pressures (ambient to 0.06 GPa) enabled us to investigate the elastic properties of halide perovskites and elpasolites in their ambient crystal structure. We find that halide perovskites and elpasolites show common trends in the bulk modulus and thermal expansivity. Both materials become softer as the halide ionic radius increases from Cl to Br to I, exhibiting higher compressibility and larger thermal expansivity. The mixed-halide compositions show intermediate properties to the pure compounds. Contrary, cations show a minor effect on the elastic properties. Finally, we observe that thermal phase transitions in *e.g.*, MAPbI₃ and CsPbCl₃ lead to a softening of the lattice, together with negative expansivity for certain crystal axes, already tens of degrees away from the transition temperature. Hence, the range in which the phase transition affects thermal and elastic properties is substantially broader than previously thought. These findings highlight the importance of considering the temperature-dependent elastic properties of these materials, since stress induced during manufacturing or temperature sweeps can significantly impact the stability and performance of the corresponding devices.

Table of Contents

Halide perovskite



Elpasolite



Introduction

Lead halide perovskite and related lead-free elpasolite (*i.e.*, double perovskite) semiconductors are widely investigated for a variety of optoelectronic applications, including photovoltaics,¹⁻⁴ light emitting diodes,^{5,6} photoredox catalysis,⁷⁻⁹ and radiation detection.¹⁰⁻¹² The unprecedented interest in this class of materials can be understood from its excellent optoelectronic performance, in combination with enormous chemical and structural flexibility. For instance, mixing halides in lead halide perovskites enables tuning the absorption onset and emission wavelength over the entire visible range of the light spectrum.¹³ In halide elpasolites, with the general formula $A_2B^I B^{III} X_6$, bandgap tunability can be obtained by mixing metals at the B^{III} -site, such as Bi, Sb, In or Fe,¹⁴⁻¹⁶ and to some extent by mixing halides (X-site).¹⁷⁻¹⁹ In contrast to the plethora of studies on optoelectronic properties and applications of halide perovskites and elpasolites, there is still limited knowledge about their mechanical properties, such as compressibility and expansivity, and how these properties vary with temperature. Additionally, little is known about the temperature-dependent crystal phases of these materials. The solution-processed deposition of halide perovskites and elpasolites in the form of thin films onto substrates involves elevated temperatures ranging from 100 to 200°C. Additionally, the differences in the structural and thermal properties of substrates and halide perovskites, such as lattice parameters, thermal expansion coefficient, can lead to strain and deformations during the thin film deposition. Previously, we and others have found that compression slows down halide migration, and that compression or strain can activate or suppress light-induced halide segregation.²⁰⁻²³ Thus, quantifying to what extent this class of relatively soft materials responds to changes in temperature and pressure leading to stress-induced deformations, is key for growing stable thin films of these perovskites and manipulating their optoelectronic properties. Previous studies that report on elastic properties used diamond anvil cells (DACs) to apply external pressure,^{22,24-30} and hence probed high pressure regimes (several to hundreds GPa) and crystal phases that are far from relevant to their ambient crystal structure. The deformations induced in halide perovskite films during the solution-processed deposition are comparable to the exertion of mild pressure (<0.5 GPa).³¹ Therefore, hydraulic pressure techniques are needed to investigate how the crystal structure would respond in the more relevant pressure range. In

this synchrotron-based powder X-ray diffraction (XRD) study, we investigated the structural properties of halide perovskites and elpasolites at pressures between 0.004 and 0.060 GPa, using a hydrostatic pressure cell. Importantly, this allowed us to determine the elastic properties of the materials in their ambient crystal structures. The pressure-dependent measurements were performed between room temperature and 90°C (298 to 363 K), a typical temperature range for thin film synthesis and photovoltaic operation conditions. We report the temperature-dependent bulk modulus for a wide variety of compositions, including MAPbCl₃, -Br₃, and -I₃ (MA = methylammonium), mixed halide variants thereof, CsPbCl₃, -Br₃, and -I₃, and the elpasolites Cs₂AgBiCl₆, -Br₆, mixed halide and trivalent metal variants thereof. Hence, we find some general trends in elastic properties of halide perovskites and elpasolites. For all perovskite and elpasolite materials, we find that the iodide-based materials are substantially softer than their bromide- and chloride-based analogues, and that the bulk modulus increases from I⁻ to Br⁻ to Cl⁻. The mixed-halide perovskites show bulk moduli in between their pure compounds and, within the same crystal phase, exhibit a linear relation with the average halide radius. In addition, the bulk modulus appears constant in the investigated temperature range for all materials, provided that the materials remain in the same crystal structure. For both CsPbCl₃ and MAPbI₃, that undergo phase transitions at around 325 and 330 K respectively, we observe a reduction of the bulk modulus at temperatures close to the phase transition. In addition, as the elastic properties of non-cubic perovskites are anisotropic, we also estimate the compressibility in different crystallographic directions. Finally, we find that some temperature-dependent phase transitions of halide perovskites are reflected in negative thermal expansion coefficients of certain crystal axes, already several tens of degree below the transition temperature. The variation of thermal expansivity with crystal axis (for non-cubic perovskites) and crystal structure (*i.e.*, temperature) could induce stress during synthesis or temperature cycling, and in turn affect the stability of the corresponding devices (*e.g.*, ion migration). Therefore, elastic properties should be considered for thin films when designing optoelectronic devices of halide perovskites.

Results and Discussion

Microcrystalline powder samples of $\text{MAPb}(\text{Cl}_{1-x}\text{Br}_x)_3$, $\text{MAPb}(\text{I}_{1-x}\text{Br}_x)_3$, CsPbCl_3 , $-\text{Br}_3$, and $-\text{I}_3$, and several elpasolites (based on Cl^- , Br^- , Bi^{3+} and/or Fe^{3+} , Sb^{3+} , In^{3+}) were made via mechanochemical synthesis in a ball mill, as described in the **Experimental Section** in the **Supporting Information**. To quantify the effect of both pressure and temperature on the structural parameters of these halide perovskites and elpasolites, we performed pressure- and temperature-dependent powder XRD measurements using a synchrotron radiation source at the European Synchrotron Radiation Facility (ESRF) beamline BM01.³² We used a hydrostatic pressure cell filled with a fluorinated inert liquid (FC-770) as a pressure-transmitting medium and we performed pressure sweeps from 0.004 to 0.060 GPa at temperatures of 298, 318, 335, and 355 K. Additional details on the experimental setup can be found in the **Experimental Section** of the **Supporting Information**. This approach enables to directly measure the variation of structural parameters as a function of pressure and temperature and thereby allows to determine material properties such as the bulk modulus (B), the compressibility (K), and thermal expansivity (α). **Figure 1a** shows selected reflections of the diffraction pattern of tetragonal ($I4/mcm$ space group) MAPbI_3 collected at 0.004 GPa and 0.060 GPa and room temperature. The external compression shifts the diffraction peaks to higher 2θ values, while the crystal phase remains constant in the range of pressures explored. **Figure 1b** shows the diffraction pattern of MAPbI_3 collected at 333 K. At this temperature, MAPbI_3 is in a cubic crystal structure ($Pm-3m$ space group). Also in this case, we observe the shift of the reflections towards higher 2θ values without indication of phase transition induced by external pressure. In **Figure 1c–d**, we plot the lattice parameters of tetragonal MAPbI_3 (room temperature, where $a = b \neq c$, **Figure 1c**), and cubic MAPbI_3 (333 K, where $a = b = c$, **Figure 1d**), as a function of external pressure. This pressure-induced variation of the lattice parameters was determined from refinements using the Rietveld method, *i.e.*, the obtained diffractograms were fitted using Pseudo-Voigt functions considering the unit cell dimensions and atomic coordinates as variables. Further details on the method are provided in the **Method Section** of the **Supporting Information**. In all cases, as expected, applying external pressure leads to a decrease in lattice parameter.

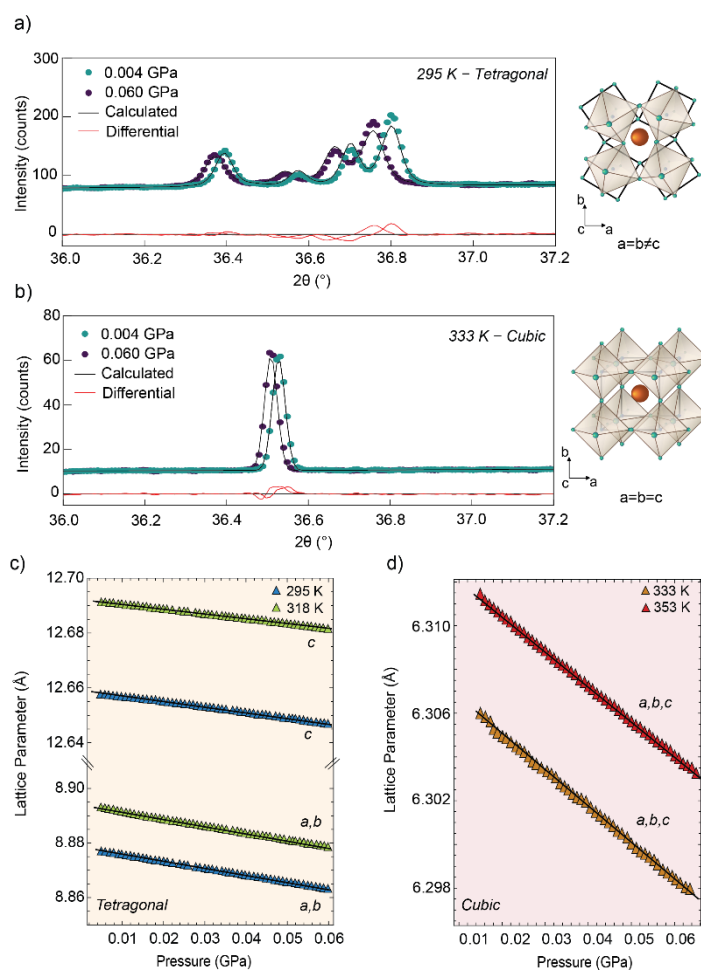


Figure 1. **a)** Selected reflections of the diffraction pattern of MAPbI₃ collected at room temperature and **b)** at 333 K, at 0.004 (green) and 0.060 GPa (purple), together with schematic drawings of the crystal structures. In black, the calculated profile structure and in red the residuals of the fit. Pressure-dependent lattice parameters of **c)** tetragonal MAPbI₃ (I4/mcm space group)³³ collected at 295 and 318 K, and **d)** cubic MAPbI₃ (Pm-3m space group) collected at 335 and 355 K obtained from refinements using the Rietveld method. Fits are shown with solid black lines.

In order to investigate the role of the halide on the temperature-dependent elastic properties, we have performed a similar analysis on the mixed-halide perovskites MAPb(Cl_{1-x}Br_x)₃ and MAPb(I_{1-x}Br_x)₃, as reported in **Figure S1–S7**. Except for MAPbI₃, which has a tetragonal (I4/mcm space group) symmetry in the range of 298 and 330 K,^{34,35} these perovskites show cubic symmetry (Pm-3m space group) under these conditions.^{22,36} For all single and mixed-halide perovskites, we observed a linear decrease of the volume with pressure for the temperatures explored. The isothermal equation of state for a solid is given by the bulk modulus, B:

$$B = \frac{\text{pressure}}{\text{strain}} = -\frac{\Delta P}{\Delta V}V \quad (1)$$

with $\Delta P/\Delta V$ the derivative of pressure with respect to volume, and V the volume at ambient pressure. By fitting this function to the pressure–volume trends (**Figure S1–S7**), we estimated the bulk moduli (B) of the single halide (iodide, bromide, chloride) and mixed-halide series $\text{MAPb}(\text{Cl}_{1-x}\text{Br}_x)_3$ and $\text{MAPb}(\text{I}_{1-x}\text{Br}_x)_3$. The results are shown in **Figure 2a** and reported in **Table S1** in **Supporting Note 1**. In the entire temperature range of 298 – 355 K, MAPbBr_3 (halide fraction $x = 1$) has a bulk modulus of 17 GPa, which gradually increases on replacing the Br^- with Cl^- . An increase of the bulk modulus is associated with an increase in the stiffness of the material. At room temperature, MAPbCl_3 has a bulk modulus of 20 GPa, which seems to be slightly lower (19 GPa) at elevated temperatures. However, over the entire temperature range, the bromide-based perovskites are significantly softer than the perovskites containing chloride. The introduction of iodide leads to further softening of the perovskites, gradually decreasing the bulk modulus to 14 GPa. This softening of the bulk modulus with larger halides is consistent with previous single crystal studies reporting smaller Young’s modulus of the $\{100\}$ crystal facet.³⁷

For the cubic systems, we observe a linear relation between the bulk modulus and the average halide radius as common for metal alloys (**Figure S8**).³⁸ Such findings confirm previous assumptions on similar compositions,²⁰ but are in contrast with theoretical predictions for $\text{CsPb}(\text{I}_{1-x}\text{Br}_x)_3$.³⁹ In order to investigate the role of the MA^+ cation in the halide perovskite and the role of the trivalent metal in the elpasolite structure on their elastic properties, we determined the temperature-dependent bulk moduli of CsPbBr_3 and $-\text{Cl}_3$, as well as bulk moduli of $\text{Cs}_2\text{AgBiBr}_6$ and $-\text{Cl}_6$, and $\text{Cs}_2\text{AgInCl}_6$. The results are shown in **Figures 2b–c** and **Figure S9–13** while numeric values are reported in **Table S1** in **Supporting Note 1**. Even though the Cs-based perovskites have different crystal structures than the MA-based ones, the room temperature bulk moduli of CsPbBr_3 ($B = 17.5$ GPa, see **Figure S12**) and $-\text{Cl}_3$ ($B = 19$ GPa, see **Figure 2c** and **Figure S13**) are almost identical to their MA-based counterparts (*i.e.*, less than 1 GPa variation). These observations suggest that the mechanical properties are mostly defined by the framework of corner-sharing PbI_3 (Cl_3 , Br_3) octahedra. Regarding the B-site cation, we observe that replacing Pb^{2+} with both Ag^+ and a trivalent cation (Bi^{3+} or In^{3+}) leads to a stiffening of the lattice,

associated with larger bulk moduli, *i.e.*, 22-23 Gpa for the ones with Cl^- and 19 Gpa for $\text{Cs}_2\text{AgBiBr}_6$.²⁶ However, the effect of changing the cations is relatively small compared to the effect of changing the halides. Hence, we can conclude that the halide framework dominates the mechanical properties of halide perovskites and elpasolites, rather than the A- or B-site cations. Another general finding is that most of the bulk moduli only show slight changes with temperature in the range from 298 to 355 K, in contrast with the expected decrease of B with temperature observed in oxide perovskites, and the expected increase calculated for tin-based halide perovskites such as CsSnI_3 .⁴⁰ As can be seen in **Figures 2a** and **Figure 2b**, the variation of the bulk modulus with the halide is larger than any temperature effect in this range. Two notable exceptions include CsPbCl_3 and MAPbI_3 , that undergo temperature-dependent phase transitions in between 298 and 330 K, shown in **Figure 2c**. Our data hint towards a softening of the materials (*i.e.*, lower bulk modulus) close to their transition temperature (dotted lines). This finding is particularly relevant since temperature-dependent elastic properties may introduce stress during fabrication of halide perovskite and elpasolite thin films or during temperature cycling processes in operating devices.

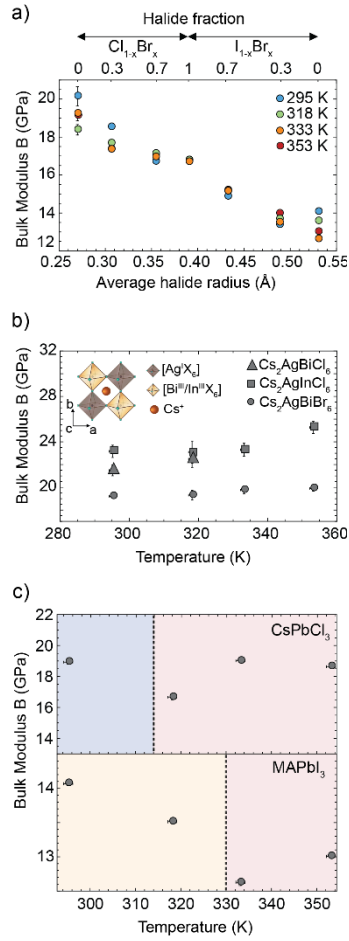


Figure 2. a) Bulk modulus (B) of methylammonium (MA) lead mixed-halide perovskites as a function of the average halide radius and the mixing halide (Cl: left, Br: middle, I: right) ratio at 295, 318, 335, 355 K. This shows that the Cl-based materials soften on the addition of Br⁻, and that I⁻ leads to further softening of the lattice. Note that, except for MAPbI₃, all these perovskites exhibit a cubic symmetry, and their bulk modulus is roughly constant with temperature. **b)** Bulk modulus of halide double perovskites Cs₂AgBiBr₆ (circle), Cs₂AgInBr₆ (square), and Cs₂AgBiCl₆ (triangle) as a function of temperature. Also here, the Cl-based compounds are stiffer than the Cs₂AgBiBr₆, with only minor temperature effects. **c)** Bulk modulus of MAPbI₃ and CsPbCl₃ as a function of temperature. The regions in blue, yellow, and red correspond to the orthorhombic, tetragonal, and cubic phase, respectively. The dashed lines correspond to the temperature at which the phase transition occurs.

Considering that the bulk modulus is a volume property, while the elastic properties of non-cubic perovskites, such as tetragonal MAPbI₃, are in general anisotropic and therefore depend on crystallographic direction, we derived the compressibility of the specific crystal axes by monitoring their compression as a function of applied pressure (*e.g.*, K_a , for the compressibility along a-axis):

$$K_a = -\frac{(a_f - a_0)}{a_f} P \quad (2)$$

with a the lattice parameter, and $a_f - a_0$ the change in lattice parameter between the lattice parameter at the final (a_f) and initial (a_0) pressure. Hence, we determined the compressibility for a -, b -, and c -axis for non-cubic perovskites. The volumetric compressibility, K_V , *i.e.*, the susceptibility of a material to compress upon external applied pressure, is inversely proportional to B and is calculated as reported in **Supporting Note 2** while values are reported in **Table S5**. The compressibility along the a -, b - and c -axis for the compositions studied are reported in **Table S2–4**. **Figure 3** shows that compression along the a - and b - axes of tetragonal MAPbI₃ and orthorhombic CsPbCl₃ is significantly larger than for the c -axis. In addition, we observe that the compressibility of c increases significantly in CsPbCl₃ during the orthorhombic-to-cubic phase transition as well as in MAPbI₃ during the tetragonal-to-cubic phase transition, as it becomes identical to the a - and b -axes. In the orthorhombic CsPbBr₃, we find that compression along the a - and c -axes is significantly larger than for the b -axis. Additional pressure studies using an extended temperature range are needed to determine the origin of the observed axis-dependent compressibility. For CsPbBr₃, we observe a gradual increase of the compressibility of the b - and c axis with temperature, in combination with swapping of the a - and b -axis compressibility at 353 K. This phenomenon may occur in the case of an anti-isostructural phase transition, although more measurements are needed to conclusively show whether such a transition exists in CsPbBr₃. In order to investigate the relation between pressure response and thermal expansivity, we further measured the temperature-dependent XRD of single-halide perovskites (MAPbI₃, MAPbBr₃, MAPbCl₃, CsPbBr₃, CsPbCl₃) and elpasolites (Cs₂AgBiBr₆, Cs₂AgBiCl₆, Cs₂AgInCl₆) between 100 and 400 K. A similar Rietveld refinement was used to study the temperature dependence of the crystal axes a , b and c . The results are shown in **Figure 4**. Here, blue areas represent orthorhombic (Pnmb space group), yellow areas represent tetragonal (I4/mcm space group), and red areas represent cubic symmetry (Pm-3m space group). Although similar experiments have been reported for a selection of these compositions,^{34,36,41,42} we here compare thermal expansivity of all compositions using identical synthesis and measurement conditions and link the thermal response to the elastic properties of the same materials.

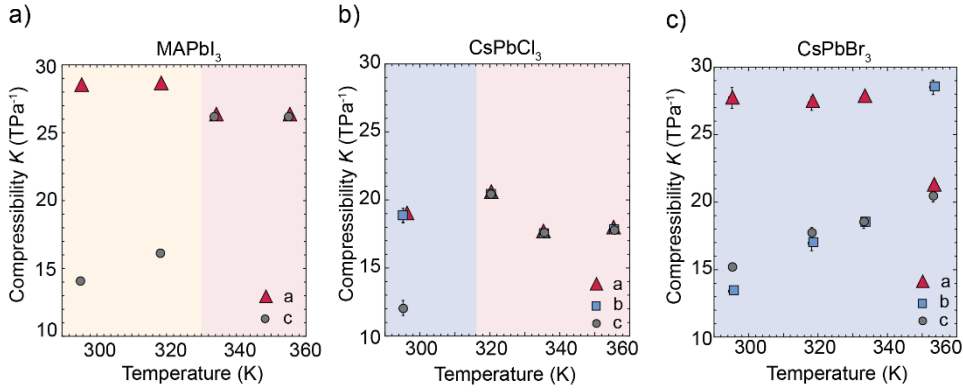


Figure 3. **a)** Compressibility K of the crystal axes in the tetragonal (yellow) and cubic (red) phase of MAPbI_3 . The compressibility of the c -axis is smaller compared to the a -axis in the tetragonal phase. **b)** Compressibility K of the crystal axes in the orthorhombic (blue) and cubic (red) phase of CsPbCl_3 . The compressibility of the c -axis is smaller compared to the a -axis and b -axis in the orthorhombic phase. **c)** Compressibility K of the crystal axes in the orthorhombic (blue) phase. The compressibility of the b -axis is smaller compared to the a - and c -axis in the tetragonal phase up to 353 K where an abrupt change is observed. At 353 K, the compressibility of the b -axis is larger than the compressibility of a - and c -axis. Error bars are reported in the figure and are in some cases smaller than the data point size.

Comparing the different halide perovskites and elpasolites in cubic symmetry (red areas), we observe an increase in lattice parameters as a function of temperature, associated with a positive thermal expansivity as shown in **Table 1**. In line with the halide-dependent trend in bulk modulus, for all compositions studied here the thermal expansivity is observed to increase following $\text{Cl} < \text{Br} < \text{I}$, due to the softness of the material. We observe that the elpasolites are less expandable with temperature than the lead-halide perovskites, with thermal expansivity of $2.86 \times 10^{-5} \text{ K}^{-1}$ for $\text{Cs}_2\text{AgBiBr}_6$ and $2.42 \times 10^{-5} \text{ K}^{-1}$ for $\text{Cs}_2\text{AgBiCl}_6$. This observation is consistent with their larger bulk moduli, showing that the elpasolite structure is more resistant to both temperature and pressure changes. Furthermore, the absolute values are close to recent theoretical predictions.⁴³

	Orthorhombic ($\times 10^{-5} \text{ K}^{-1}$)		Tetragonal ($\times 10^{-5} \text{ K}^{-1}$)		Cubic ($\times 10^{-5} \text{ K}^{-1}$)
MAPbI₃	a	3.81	a=b	Function*	4.04
	b	2.02			
	c	5.81	c	0.34	
MAPbBr₃	a	9.04	a=b	6.99	3.53
	b	-2.79			
	c	1.00	c	Function*	
MAPbCl₃	a	Function*	-		3.51
	b	Function*			
	c	Function*			
CsPbBr₃	a	7.68	-		3.27**
	b	Function*			
	c	3.51			
CsPbCl₃	a	Function*	-		3.02
	b	Function*			
	c	Function*			
Cs₂AgBi(Br_{0.33}I_{0.67})₆	-	-	-	-	5.08**
Cs₂AgBiBr₆	-	-	-	-	2.86
Cs₂AgBiCl₆	-	-	-	-	2.42
Cs₂AgInCl₆	-	-	-	-	2.49
Cs₂Ag(Bi_{0.5}In_{0.5})Br₆	-	-	-	-	2.84**
Cs₂Ag(Bi_{0.5}Sb_{0.5})Br₆	-	-	-	-	3.34**
Cs₂Ag(Bi_{0.9}Fe_{0.1})Br₆	-	-	-	-	3.16**

*Non-linear expansivity (see **Supporting Note 3**).

**Data collected with a lab-based X-ray diffractometer.

Table 1. Thermal expansivity along all crystal axes for all compositions. If the temperature response is non-linear the experimental data is fitted using a second order polynomial and denoted by ‘Function’. The optimized parameters of these fits are given in the **Supporting Information** (see **Supporting Note 3**). As the temperature range in which the materials are orthorhombic, tetragonal, or cubic varies with composition, the reported (functions of) thermal expansivity are only valid in that specific temperature range.

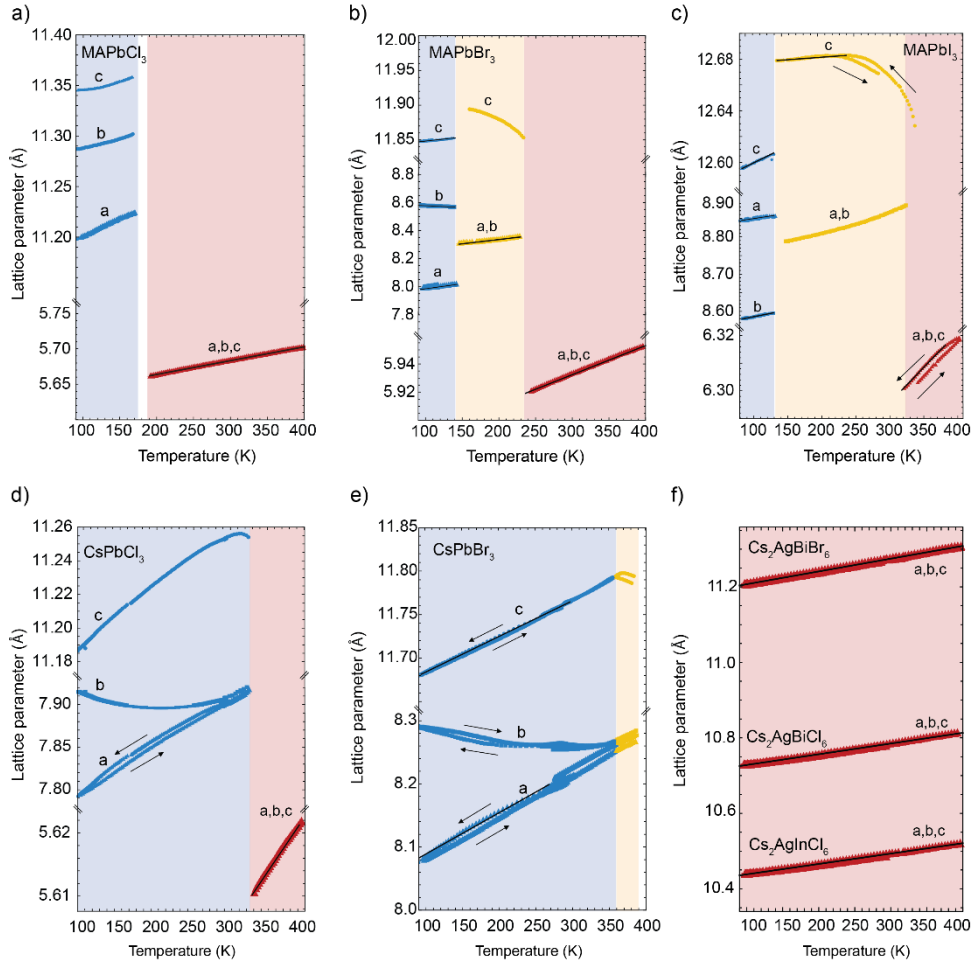


Figure 4. Temperature-dependent lattice parameters of **a)** MAPbCl₃, **b)** MAPbBr₃, **c)** MAPbI₃, **d)** CsPbCl₃, **e)** CsPbBr₃ and **f)** Cs₂AgBiBr₆, Cs₂AgBiCl₆, Cs₂AgInCl₆ obtained from profile Rietveld refinement of synchrotron XRD patterns collected between 90 K and 400 K. The blue, yellow and red regions correspond to the orthorhombic, tetragonal and cubic phase, respectively. The regions in white correspond to the temperature range where two phases coexist in the XRD patterns. The black arrows indicate the direction of temperature variation, *i.e.* cooling (arrow down) and heating (arrow up). Solid lines represent the fit for the linear thermal expansivity.

Additional lab-based temperature-dependent XRD on elpasolite with mixed trivalent metals, *i.e.*, Cs₂Ag(Bi_{0.5}Sb_{0.5})Br₆, Cs₂Ag(Bi_{0.5}In_{0.5})Br₆, Cs₂Ag(Bi_{0.9}Fe_{0.1})Br₆, and mixed-halide such as Cs₂AgBi(Br_{0.33}I_{0.67})₆, (**Supporting Note 4** and **Figure S14**) indicate higher thermal expansivity for elpasolites containing I⁻ ions, identical to the lead-based perovskites (see **Table 1**). Previous work already showed a minor role of the Cs cation on the thermal expansivity in halide elpasolites,⁴⁴ and we here find that also the metal cation does not affect the thermal expansivity. For phases with lower symmetry than cubic, *i.e.*, orthorhombic (blue) and tetragonal (yellow), thermal expansivity is anisotropic. Interestingly, the axes-dependent thermal expansivity and compressibility in tetragonal

crystal structure follow the same trend (*i.e.*, *c*-axis is less expandable and more compressible compared to axis *a* and *b*). On the other hand, in the orthorhombic crystal phase we observe no such relation suggesting that thermal expansivity and compressibility are decoupled in this phase. An additional consideration is that some lattice parameters have non-linear temperature dependent thermal expansivity. For example, the axes of orthorhombic CsPbBr₃ and CsPbCl₃ and of tetragonal MAPbI₃, show a non-linear dependence of lattice parameter with temperature, so that the thermal expansivity becomes temperature-dependent (see **Supporting Note 3** and **Table S6**). Notably, in all halide perovskites studied here, the *c*-axis of the tetragonal phase has a negative thermal expansivity in at least a part of the temperature range. According to Landau theory such a behavior reflects bi-linear coupling of the order parameter and spontaneous lattice strain.⁴⁵ Considering that negative thermal expansivity values (*i.e.*, thermal contraction) are mainly observed at temperatures ‘close’ to thermal phase transitions, it seems likely that these two phenomena are related. Previous work has reported similar behavior for MAPbI₃ and formamidinium lead iodide (FAPbI₃) perovskites^{46–48} as well as several oxide-based materials that undergo phase transitions.⁴⁹ For CsPbBr₃ and CsPbCl₃, the temperature range with negative thermal expansivity for the *c*-axis is relatively small (20–40 K). In contrast, for MAPbBr₃ and MAPbI₃, the negative thermal expansivity of the *c*-axis is already observed 100 K below the tetragonal-cubic phase transition. This observation, together with temperature-dependent bulk modulus from **Figure 2a**, shows that the range in which the phase transition is affecting thermal and elastic properties is substantially broader than previously thought on basis of the (much smaller) temperature range in which crystal phases co-exist.³⁴ This has major implications for synthesizing thin films on substrates with different thermal expansivity than those exhibited by the perovskite, where the temperature gradient during cooling from annealing to room temperature will introduce strain in the material.

Conclusions

We determined temperature-dependent elastic properties of several halide perovskites (namely single- and mixed-halide) and elpasolite (namely mixed halide and mixed trivalent metals) from pressure- and temperature-dependent diffraction experiments using a synchrotron radiation source. We used temperatures ranging from 298 to 363 K (*i.e.*, ambient to 90°C), which is a typical temperature range for thin film synthesis and photovoltaic operation conditions. To obtain information relevant to ambient phases, we explored pressures from ambient to 0.06 GPa. We find that the elastic properties and the thermal expansivity in both halide perovskites and elpasolites are dominated by the halide framework, with lower bulk moduli for larger halide radius size ($\text{Cl} < \text{Br} < \text{I}$). Contrary, the monovalent cation and the trivalent metal have a minor role in determining elastic properties. The bulk modulus of these materials remains constant within the investigated temperature range, provided that the crystal structure remains unchanged. On the other hand, we observe that thermal phase transitions lead to a decrease in the bulk modulus (*i.e.*, softening of the material), as exemplified by MAPbI_3 and CsPbCl_3 . For non-cubic systems, where the elastic properties are anisotropic, we obtained the axes-dependent compressibility. Our results suggest that the c axis is much softer than the a - and b axes in the tetragonal MAPbI_3 and orthorhombic CsPbCl_3 , whereas the b -axis is softer in CsPbBr_3 . Furthermore, we find that some temperature-dependent phase transitions of halide perovskites are accompanied by negative thermal expansivity of certain crystal axes, already several tens of degree below the phase transition temperature. This observation shows that the range in which the phase transition is affecting thermal and elastic properties is substantially broader than previously thought on basis of the (much smaller) temperature range in which phases co-exist. Altogether, these findings have major implications for synthesizing thin films at substrates with different thermal expansivities than the perovskite and elpasolite, where the temperature gradient during the synthesis and the temperature cycling during device operation will introduce strain in the material. Hence, acquiring a deep comprehension of the temperature-dependent elastic properties in these materials is essential to bolster the advancements in strain engineering which has proven to be a potent tool for manipulating both the optical properties and the stability of perovskite thin films.

Supporting Information

Experimental details, materials, and methods; lattice parameters as a function of pressure, P-V curves, temperature-dependent bulk moduli and axes-dependent compressibility for all the compositions explored; *in-situ* temperature-dependent XRD of several elpasolites; tables including temperature-dependent bulk moduli, axes-dependent compressibility and temperature-dependent expansivity; lab-based temperature dependent X-ray diffraction for additional elpasolites; calculation of volumetric and axes-dependent thermal expansivity and compressibility; calculation of the bulk moduli. Data and fit procedures reported in this study can be accessed at <https://doi.org/XXX> and are available under a CC-BY Creative Commons Attribution 4.0 International license.

Acknowledgments

E.M.H. thanks the Dutch Research Council for funding under the grant number VI.Veni.192.034. L.A.M. acknowledges funding from the Dutch Research Council (NWO) under the grant number OCENW.XS22.2.039. B.B. acknowledges funding by the Austrian Science Fund (FWF) under the project number J4607-N. Prof. Bert Weckhuysen is gratefully acknowledged for facilitating the supporting *in-situ* XRD measurements. The authors acknowledge the European Synchrotron Radiation Facility (ESRF) for provision of synchrotron radiation beamtime at the Swiss-Norwegian beamline BM01 (proposal MA5378). The authors acknowledge funding from the Advanced Research Center Chemical Building Blocks Consortium (ARC CBBC).

References

- (1) Greul, E.; Petrus, M. L.; Binek, A.; Docampo, P.; Bein, T. Highly Stable, Phase Pure Cs₂AgBiBr₆ Double Perovskite Thin Films for Optoelectronic Applications. *J. Mater. Chem. A* **2017**, *5* (37), 19972–19981.
- (2) Zhang, Z.; Sun, Q.; Lu, Y.; Lu, F.; Mu, X.; Wei, S.; Sui, M. Hydrogenated Cs₂AgBiBr₆ for Significantly Improved Efficiency of Lead-Free Inorganic Double Perovskite Solar Cell. *Nat. Commun.* **2022**, No. 13, 3397.
- (3) Stranks, S. D.; Eperon, G. E.; Grancini, G.; Menelaou, C.; Alcocer, M. J. P.; Leijtens, T.; Herz, L. M.; Petrozza, A.; Snaith, H. J. Electron-Hole Diffusion Lengths Exceeding 1 Micrometer in an Organometal Trihalide Perovskite Absorber. *Science* **2013**, *342* (6156), 341–344.
- (4) Zhang, H.; Ji, X.; Yao, H.; Fan, Q.; Yu, B.; Li, J. Review on Efficiency Improvement Effort of Perovskite Solar Cell. *Sol. Energy* **2022**, *233* (January), 421–434.
- (5) Song, J.; Li, J.; Li, X.; Xu, L.; Dong, Y.; Zeng, H. Quantum Dot Light-Emitting Diodes Based on Inorganic Perovskite Cesium Lead Halides (CsPbX₃). *Adv. Mater.* **2015**, *27* (44), 7162–7167.
- (6) Yang, D.; Zhao, B.; Yang, T.; Lai, R.; Lan, D.; Friend, R. H.; Di, D. Toward Stable and Efficient Perovskite Light-Emitting Diodes. *Adv. Funct. Mater.* **2022**, *32* (9).
- (7) Song, X.; Wei, G.; Sun, J.; Peng, C.; Yin, J.; Zhang, X.; Jiang, Y.; Fei, H. Overall Photocatalytic Water Splitting by an Organolead Iodide Crystalline Material. *Nat. Catal.* **2020**.
- (8) Zhu, X.; Lin, Y.; Sun, Y.; Beard, M. C.; Yan, Y. Lead-Halide Perovskites for Photocatalytic α -Alkylation of Aldehydes. *J. Am. Chem. Soc.* **2019**, *141* (2), 733–738.
- (9) Zhang, Z.; Liang, Y.; Huang, H.; Liu, X.; Li, Q.; Chen, L.; Xu, D. Stable and Highly Efficient Photocatalysis with Lead-Free Double-Perovskite of Cs₂AgBiBr₆. *Angew. Chem. - Int. Ed.* **2019**, *58* (22), 7263–7267.
- (10) Wei, H.; Fang, Y.; Mulligan, P.; Chuirazzi, W.; Fang, H.-H.; Wang, C.; Ecker, B. R.; Gao, Y.; Loi, M. A.; Cao, L.; Huang, J. Sensitive X-Ray Detectors Made of Methylammonium Lead Tribromide Perovskite Single Crystals. *Nat. Photonics* **2016**, *10*, 333–339.
- (11) Yakunin, S.; Sytnyk, M.; Kriegner, D.; Shrestha, S.; Richter, M.; Matt, G. J.; Azimi, H.; Brabec, C. J.; Stangl, J.; Kovalenko, M. V.; Heiss, W. Detection of X-Ray Photons by Solution-Processed Lead Halide Perovskites. *Nat. Photonics* **2015**, *9* (7), 444–449.
- (12) Steele, J. A.; Pan, W.; Martin, C.; Keshavarz, M.; Debroye, E.; Yuan, H.; Banerjee, S.; Fron, E.; Jonckheere, D.; Kim, C. W.; Baekelant, W.; Niu, G.; Tang, J.; Vanacken, J.; Van der Auweraer, M.; Hofkens, J.; Roeffaers, M. B. J. Photophysical Pathways in Highly Sensitive Cs₂AgBiBr₆ Double-Perovskite Single-Crystal X-Ray Detectors. *Adv. Mater.* **2018**, *1804450*, 1–7.
- (13) Park, B. W.; Philippe, B.; Jain, S. M.; Zhang, X.; Edvinsson, T.; Rensmo, H.; Zietz, B.; Boschloo, G. Chemical Engineering of Methylammonium Lead Iodide/Bromide Perovskites: Tuning of Opto-Electronic Properties and Photovoltaic Performance. *J. Mater. Chem. A* **2015**, *3* (43), 21760–21771.
- (14) Du, K.; Meng, W.; Wang, X.; Yan, Y.; Mitzi, D. B. Bandgap Engineering of Lead-Free Double Perovskite Cs₂AgBiBr₆ through Trivalent Metal Alloying. *Angew. Chem. - Int. Ed.* **2017**, *56* (28), 8158–8162.
- (15) Hutter, E. M.; Gélvez-Rueda, M. C.; Bartesaghi, D.; Grozema, F. C.; Savenije, T. J. Band-Like Charge Transport in Cs₂AgBiBr₆ and Mixed Antimony-Bismuth Cs₂AgBi_{1-x}Sb_xBr₆ Halide Double Perovskites. *ACS Omega* **2018**, *3* (9), 11655–11662.

- (16) Ji, F.; Wang, F.; Kobera, L.; Abbrent, S.; Brus, J.; Ning, W.; Gao, F. The Atomic-Level Structure of Bandgap Engineered Double Perovskite Alloys Cs₂AgIn_{1-x}FexCl₆. *Chem. Sci.* **2021**, *12* (5), 1730–1735.
- (17) Dakshinamurthy, A. C.; Gupta, M.; Nanda, B. R. K.; Sudakar, C. Anionic Alloying in Hybrid Halide Cs₂AgBiBr₆-XCl_x Double Perovskites: Is It True Alloying or Preferential Occupation of Halide Ions in MX₆ Octahedra? *J. Phys. Chem. C* **2022**.
- (18) Gray, M. B.; McClure, E. T.; Woodward, P. M. Cs₂AgBiBr₆-XCl_x Solid Solutions – Band Gap Engineering with Halide Double Perovskites. *J. Mater. Chem. C* **2019**, *7*, 9686–9689.
- (19) Wu, H.; Erbing, A.; Johansson, M. B.; Wang, J.; Kamal, C.; Odelius, M.; Johansson, E. M. J. Mixed-Halide Double Perovskite Cs₂AgBiX₆ (X=Br, I) with Tunable Optical Properties via Anion Exchange. *ChemSusChem* **2021**, *14* (20), 4507–4515.
- (20) Hutter, E. M.; Muscarella, L. A.; Wittmann, F.; Versluis, J.; McGovern, L.; Bakker, H. J.; Woo, Y.-W. W.; Jung, Y.-K. K.; Walsh, A.; Ehrler, B. Thermodynamic Stabilization of Mixed-Halide Perovskites against Phase Segregation. *Cell Reports Phys. Sci.* **2020**, *1* (8), 100120.
- (21) Muscarella, L. A.; Hutter, E. M.; Wittmann, F.; Woo, Y. W.; Jung, Y.-K.; McGovern, L.; Versluis, J.; Walsh, A.; Bakker, H. J.; Ehrler, B. Lattice Compression Increases the Activation Barrier for Phase Segregation in Mixed-Halide Perovskites. *ACS Energy Lett.* **2020**, *5* (10), 3152–3158.
- (22) Jaffe, A.; Lin, Y.; Beavers, C. M.; Voss, J.; Mao, W. L.; Karunadasa, H. I. High-Pressure Single-Crystal Structures of 3D Lead-Halide Hybrid Perovskites and Pressure Effects on Their Electronic and Optical Properties. *ACS Cent. Sci.* **2016**, *2* (4), 201–209.
- (23) Zhao, Y.; Miao, P.; Elia, J.; Hu, H.; Wang, X.; Heumueller, T.; Hou, Y.; Matt, G. J.; Osvet, A.; Chen, Y. T.; Tarragó, M.; de Ligny, D.; Przybilla, T.; Denninger, P.; Will, J.; Zhang, J.; Tang, X.; Li, N.; He, C.; Pan, A.; Meixner, A. J.; Spiecker, E.; Zhang, D.; Brabec, C. J. Strain-Activated Light-Induced Halide Segregation in Mixed-Halide Perovskite Solids. *Nat. Commun.* **2020**, *11* (1), 1–9.
- (24) Jaffe, A.; Lin, Y.; Karunadasa, H. I. Halide Perovskites under Pressure: Accessing New Properties through Lattice Compression. *ACS Energy Lett.* **2017**, *2* (7), 1549–1555.
- (25) Lv, C.; Yang, X.; Shi, Z.; Wang, L.; Sui, L.; Li, Q.; Qin, J.; Liu, K.; Zhang, Z.; Li, X.; Lou, Q.; Yang, D.; Zang, J.; Liu, R.; Liu, B.; Shan, C. X. Pressure-Induced Ultra-Broad-Band Emission of a Cs₂AgBiBr₆ Perovskite Thin Film. *J. Phys. Chem. C* **2020**, *124* (2), 1732–1738.
- (26) Dong, L.; Sun, S.; Deng, Z.; Li, W.; Wei, F.; Qi, Y.; Li, Y.; Li, X.; Lu, P.; Ramamurty, U. Elastic Properties and Thermal Expansion of Lead-Free Halide Double Perovskite Cs₂AgBiBr₆. *Comput. Mater. Sci.* **2018**, *141*, 49–58.
- (27) Girdzis, S. P.; Lin, Y.; Leppert, L.; Slavney, A. H.; Park, S.; Chapman, K. W.; Karunadasa, H. I.; Mao, W. L. Revealing Local Disorder in a Silver-Bismuth Halide Perovskite upon Compression. *J. Phys. Chem. Lett.* **2021**, *12* (1), 532–536.
- (28) Zhang, L.; Wang, L.; Wang, K.; Zou, B. Pressure-Induced Structural Evolution and Optical Properties of Metal-Halide Perovskite CsPbCl₃. *J. Phys. Chem. C* **2018**, *122* (27), 15220–15225.
- (29) Ke, F.; Wang, C.; Jia, C.; Wolf, N. R.; Yan, J.; Niu, S.; Devereaux, T. P.; Karunadasa, H. I.; Mao, W. L.; Lin, Y. Preserving a Robust CsPbI₃ Perovskite Phase via Pressure-Directed Octahedral Tilt. *Nat. Commun.* **2021**, No. 12, 461.
- (30) Ghebouli, M. A.; Chihi, T.; Ghebouli, B.; Fatmi, M. Study of the Structural, Elastic, Electronic and Optical Properties of Lead Free Halide Double Perovskites Cs₂AgBiX₆ (X = Br, Cl).

- Chinese J. Phys.* **2018**, *56* (1), 323–330.
- (31) Xue, D. J.; Hou, Y.; Liu, S. C.; Wei, M.; Chen, B.; Huang, Z.; Li, Z.; Sun, B.; Proppe, A. H.; Dong, Y.; Saidaminov, M. I.; Kelley, S. O.; Hu, J. S.; Sargent, E. H. Regulating Strain in Perovskite Thin Films through Charge-Transport Layers. *Nat. Commun.* **2020**, *11* (1).
 - (32) Dyadkin, V.; Pattison, P.; Dmitriev, V.; Chernyshov, D. A New Multipurpose Diffractometer PILATUS@SNBL. *J. Synchrotron Rad.* **2016**, *23*, 825–829.
 - (33) Comin, R.; Crawford, M. K.; Said, A. H.; Herron, N.; Guise, W. E.; Wang, X.; Whitfield, P. S.; Jain, A.; Gong, X.; McGaughey, A. J. H.; Sargent, E. H. Lattice Dynamics and the Nature of Structural Transitions in Organolead Halide Perovskites. *Phys. Rev. B* **2016**, *94* (9), 094301.
 - (34) Osherov, A.; Hutter, E. M.; Galkowski, K.; Brenes, R.; Maude, D. K.; Nicholas, R. J.; Plochocka, P.; Bulovic, V.; Savenije, T. J.; Stranks, S. D. The Impact of Phase Retention on the Structural and Optoelectronic Properties of Metal Halide Perovskites. *Adv. Mater.* **2016**, *28*, 10757–10763.
 - (35) Poglitsch, a.; Weber, D. Dynamic Disorder in Methylammoniumtrihalogenoplumbates (II) Observed by Millimeter-Wave Spectroscopy. *J. Chem. Phys.* **1987**, *87*, 6373.
 - (36) Lehmann, F.; Franz, A.; Többens, D. M.; Levenco, S.; Unold, T.; Taubert, A.; Schorr, S. The Phase Diagram of a Mixed Halide (Br, I) Hybrid Perovskite Obtained by Synchrotron X-Ray Diffraction. *RSC Adv.* **2019**, *9* (20), 11151–11159.
 - (37) Sun, S.; Fang, Y.; Kieslich, G.; White, T. J.; Cheetham, A. K. Mechanical Properties of Organic-Inorganic Halide Perovskites, CH₃NH₃PbX₃ (X = I, Br and Cl), by Nanoindentation. *J. Mater. Chem. A* **2015**, *3* (36), 18450–18455.
 - (38) Li, C.; Wu, P. Correlation of Bulk Modulus and the Constituent Element Properties of Binary Intermetallic Compounds. *Chem. Mater.* **2001**, *13* (12), 4642–4648.
 - (39) Saleev, V.; Shipilova, A. Ab Initio Study of Optical and Bulk Properties of Cesium Lead Halide Perovskite Solid Solutions. *Mod. Phys. Lett. B* **2019**, *33*, 1950386.
 - (40) Da Silva, E. L.; Skelton, J. M.; Parker, S. C.; Walsh, A. Phase Stability and Transformations in the Halide Perovskite CsSnI₃. *Phys. Rev. B - Condens. Matter Mater. Phys.* **2015**, *91* (14), 1–12.
 - (41) Van De Goor, T. W. J.; Liu, Y.; Feldmann, S.; Bouelle, S. A.; Neumann, T.; Winkler, T.; Kelly, N. D.; Liu, C.; Jones, M. A.; Emge, S. P.; Friend, R. H.; Monserrat, B.; Deschler, F.; Dutton, S. E. Impact of Orientational Glass Formation and Local Strain on Photo-Induced Halide Segregation in Hybrid Metal-Halide Perovskites. *J. Phys. Chem. C* **2021**, *125* (27), 15025–15034.
 - (42) Jacobsson, T. J.; Schwan, L. J.; Ottosson, M.; Hagfeldt, A.; Edvinsson, T. Determination of Thermal Expansion Coefficients and Locating the Temperature-Induced Phase Transition in Methylammonium Lead Perovskites Using X-Ray Diffraction. *Inorg. Chem.* **2015**, *54* (22), 10678–10685.
 - (43) Mu, H.; Zhang, Y.; Zou, H.; Tian, F.; Fu, Y.; Zhang, L. Physical Mechanism and Chemical Trends in the Thermal Expansion of Inorganic Halide Perovskites. *J. Phys. Chem. Lett.* **2023**, *14* (1), 190–198.
 - (44) Keshavarz, M.; Debroye, E.; Ottesen, M.; Martin, C.; Zhang, H.; Fron, E.; Küchler, R.; Steele, J. A.; Bremholm, M.; Van de Vondel, J.; Wang, H. I.; Bonn, M.; Roeffaers, M. B. J.; Wiedmann, S.; Hofkens, J. Tuning the Structural and Optoelectronic Properties of Cs₂AgBiBr₆ Double-Perovskite Single Crystals through Alkali-Metal Substitution. *Adv. Mater.* **2020**, *32* (40), 1–10.

- (45) Carpenter, M. E.; Salje, E. K. H.; Graeme-Barber, A. Spontaneous Strain as a Determinant of Thermodynamic Properties for Phase Transitions in Minerals. *Eur. J. Mineral.* **1998**, *10*, 621–691.
- (46) Keshavarz, M.; Ottesen, M.; Wiedmann, S.; Wharmby, M.; Kuchler, R.; Yuan, H.; Debroye, E.; Steele, J. A.; Martens, J.; Hussey, N. E.; Bremholm, M.; Roeffaers, M. B. J.; Hofkens, J. Tracking Structural Phase Transitions in Lead-Halide Perovskites by Means of Thermal Expansion. *Adv. Mater.* **2019**, *31* (24), 1–8.
- (47) Heiderhoff, R.; Haeger, T.; Pourdavoud, N.; Hu, T.; Al-Khafaji, M.; Mayer, A.; Chen, Y.; Scheer, H. C.; Riedl, T. Thermal Conductivity of Methylammonium Lead Halide Perovskite Single Crystals and Thin Films: A Comparative Study. *J. Phys. Chem. C* **2017**, *121* (51), 28306–28311.
- (48) Chem, J. M.; Haeger, T.; Heiderhoff, R.; Riedl, T. Thermal Properties of Metal-Halide Perovskites. *J. Mater. Chem. C* **2020**, No. 8, 14289.
- (49) Korthuis, V.; Khosrovani, N.; Sleight, A. W.; Roberts, N.; Dupree, R.; Warren, W. W. Negative Thermal Expansion and Phase Transitions in the ZrV₂-XPxO₇ Series. *Chem. Mater.* **1995**, *7* (2), 412–417.

Supporting Information to

Which Ion Dominates Temperature and Pressure Response of Halide Perovskites and Elpasolites?

Loreta A. Muscarella,^{1##} Huygen J. Jöbsis,^{1#} Bettina Baumgartner,¹ P. Tim Prins,¹ D. Nicolette Maaskant,¹ Andrei V. Petukhov,² Dmitry Chernyshov,³ Charles J. McMonagle,³ and Eline M. Hutter^{1*}

1. Inorganic Chemistry and Catalysis group, Debye Institute for Nanomaterials Science and Institute for Sustainable and Circular Chemistry, Department of Chemistry, Utrecht University, Princetonlaan 8, 3584 CB Utrecht, the Netherlands
2. Physical and Colloid Chemistry, Debye Institute for Nanomaterials Science, Department of Chemistry, Utrecht University, Padualaan 8, 3584 CH Utrecht, the Netherlands
3. Swiss–Norwegian Beamlines, European Synchrotron Radiation Facility, 71 Avenue des Martyrs, 38000 Grenoble, France

These authors contributed equally

* Correspondence should be addressed to E.M.Hutter@uu.nl and loretaangela.muscarella@gmail.com

Experimental Section

Materials

The perovskite and elpasolite powders are prepared using lead (II) iodide (PbI_2 ; TCI, purity 99.99%, trace metals basis), methylamine hydroiodide (MAI; TCI, purity >99%), lead (II) bromide (TCI, purity 98%), and methylamine hydrobromide (MABr; purity TCI, >98%), lead (II) chloride (PbCl_2 ; TCI, purity >99%) and methylamine hydrochloride (MACl; TCI, purity >98%), cesium iodide (CsI; TCI, purity > 99%), cesium bromide (CsBr; TCI, purity > 99%), cesium chloride (CsCl; TCI, purity > 99%), silver (I) chloride (AgCl ; Merck, purity 99.999% trace metals basis), silver (I) bromide (AgBr ; Alfa Aesar, Premion®, purity 99.998% metals basis), bismuth (III) iodide (BiI_3 , Merck, purity 99%), bismuth (III) bromide (BiBr_3 ; Merck, purity $\geq 98\%$), bismuth (III) chloride (BiCl_3 ; Merck, purity 99.998% trace metals basis), indium (III) bromide (InBr_3 , Alfa Aesar, purity 99.99% (metal basis)), indium (III) chloride (InCl_3 ; TCI, purity >99.0%) and, antimony (III) bromide (SbBr_3 , Alfa Aesar, purity ultra-dry 99.999% (metal basis)), iron (III) bromide (FeBr_3 , Alfa Aesar, purity >98%). The precursor powders are obtained weighing the components with the desired molar stoichiometric ratio without further purification.

Perovskite powder preparation

Methylammonium-based perovskite powders are prepared using mechanochemical synthesis by grinding the precursor salts in a ball mill (Retsch Ball Mill MM-400) using a grinding jar of 10 ml and two stainless steel balls ($\varnothing 10$ mm) for 60 minutes at 30 Hz. CsPbX_3 ($X = \text{I, Br, Cl}$) and elpasolite powders are prepared milling at 30 Hz for 90 minutes. No annealing is performed after the mechanochemical synthesis.

Pressure and temperature dependent powder X-ray diffraction

Pressure and temperature dependent powder X-ray diffraction data were collected at the Swiss–Norwegian Beamline BM01 (ESRF, Grenoble), with a $\lambda = 0.9590 \text{ \AA}$.¹ The powdered samples were loaded into a sapphire capillary pressure cell with a 1 mm external and 0.6 mm internal diameter (CRYTUR, spol. S r.o., Czech Republic).² The pressure cell was filled with a fluorinated inert liquid (FC-770, 3M) as a pressure-transmitting medium and the pressure was swept from 0.004 to 0.060 GPa at temperatures of 298, 318, 335, and 355 K. Temperature control is obtained with an Oxford Cryosystems cooler,³ where the temperature offset caused by the large diameter sapphire capillary was calibrated using the diffraction pattern of silver.⁴ The Dectris Pilatus 2 M detector was used for recording 2D diffraction images and the local program Bubble was used for integration of the 2D images.¹

Temperature-dependent, lab-based X-Ray diffraction

The additional temperature-dependent X-ray diffractograms were collected using a Bruker Axs D8 Phaser Advanced. Equipped with a Cu $K_{\alpha 1,2}$ ($\lambda = 1.54184 \text{ \AA}$) radiation source operating at 40 kV and 40 mA and an Anton Paar XRK900 Temperature Chamber. The sample height for all experiments was aligned so that the (400) reflection of $\text{Cs}_2\text{AgBiBr}_6$ was detected at 31.7° . The temperature was calibrated by measuring the lattice expansivity of MgO. For CsPbBr_3 the additional diffractograms were collected from 330 K to 500 K (and back) with a temperature increment of 1 K. The additional elpasolite compositions were studied between 325 K and 450 K as discussed in See **Supporting Note 4**.

Rietveld Refinement method

The refinements using the Rietveld method was performed using the FullProfSuite software. All diffractograms were fitted using Pseudo–Voigt functions with the unit cell dimensions, reflection intensity, atomic coordinates of the inorganic elements as variables. In some cases the Debye–Waller factor and the profile shape were used as variables to improve the quality of the fits. Note that including these variables only lower the residuals, without changing the lattice parameters obtained from the fits. The starting crystallographic information are obtained using files (CIF) retrieved from the ICSD database. Below a list of the used entries is given.

Composition, phase(s)	ICSD entry/entries
MAPbI_3 , orthorhombic, tetragonal, cubic	428898, 238610, 7236651
MAPbBr_3 , orthorhombic, tetragonal, cubic	268782, 268779, 268785
MAPbCl_3 , orthorhombic, tetragonal, cubic	1469989**, 7236651
$\text{MAPb}(\text{Br}_{0.30}\text{I}_{0.70})_3$	243598**
$\text{MAPb}(\text{Br}_{0.70}\text{I}_{0.30})_3$	243598**
$\text{MAPb}(\text{Cl}_{0.30}\text{I}_{0.70})_3$	243598**
$\text{MAPb}(\text{Cl}_{0.70}\text{I}_{0.30})_3$	243598**
CsPbBr_3 , orthorhombic, tetragonal, cubic	14608, 14610

CsPbCl ₃ , orthorhombic, cubic	230496, 249888, 29072
Cs ₂ AgBi(Br _{0.33} I _{0.67}) ₆ , cubic	252164**
Cs ₂ AgBiBr ₆ , cubic	252164
Cs ₂ AgBiCl ₆ , cubic	252451
Cs ₂ AgInCl ₆ , cubic	257115
Cs ₂ Ag(Bi _{0.5} In _{0.5})Br ₆ , cubic	252164**
Cs ₂ Ag(Bi _{0.5} Sb _{0.5})Br ₆ , cubic	252164**
Cs ₂ Ag(Bi _{0.9} Fe _{0.1})Br ₆ , cubic	252164**

** For these compositions, no structural files (.cif) were available. In these cases we have used cif's of identical structures and space groups to refine the lattice parameters. For MAPbCl₃, we have utilized the structural file of cubic MAPbI₃ (ICSD 7236651). For the MA-based mixed halide compositions, we have used the structural file of MAPb(Br_{0.15}I_{0.85})₃ (ICSD 243598). For elpasolites with mixed trivalent cations, we have utilized the structural file of cubic Cs₂AgBiBr₆ (ICSD 252164). Here, we assumed stoichiometric occupancy on the metal site, which may introduce some discrepancies in fitting the relative peak heights.

Supporting Figures

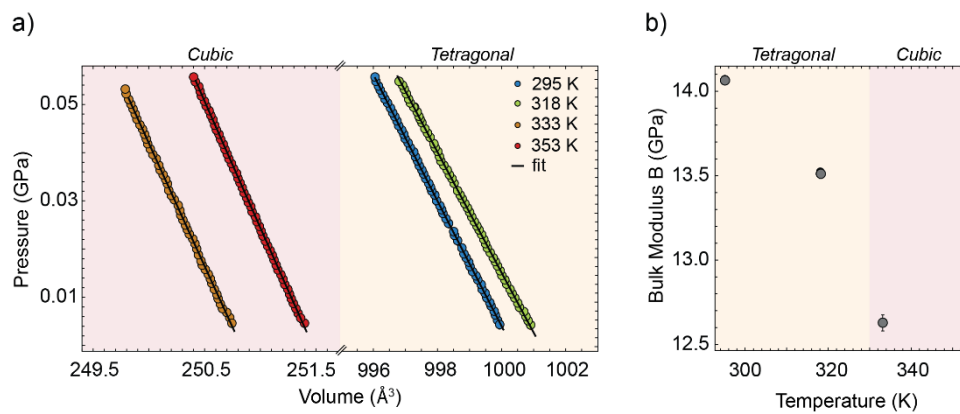


Figure S1. a) Unit-cell volume changes with pressure for MAPbI_3 in the tetragonal $I4/mcm$ (yellow) and cubic $Pm-3m$ (red) phase and the corresponding fit to equation 1 of the main text. **b)** Bulk moduli obtained from the data shown in (a) and reported as a function of temperature in the tetragonal (yellow) and cubic (red) phase. The lattice parameters versus pressure are shown in **Figure 1** of the main text.

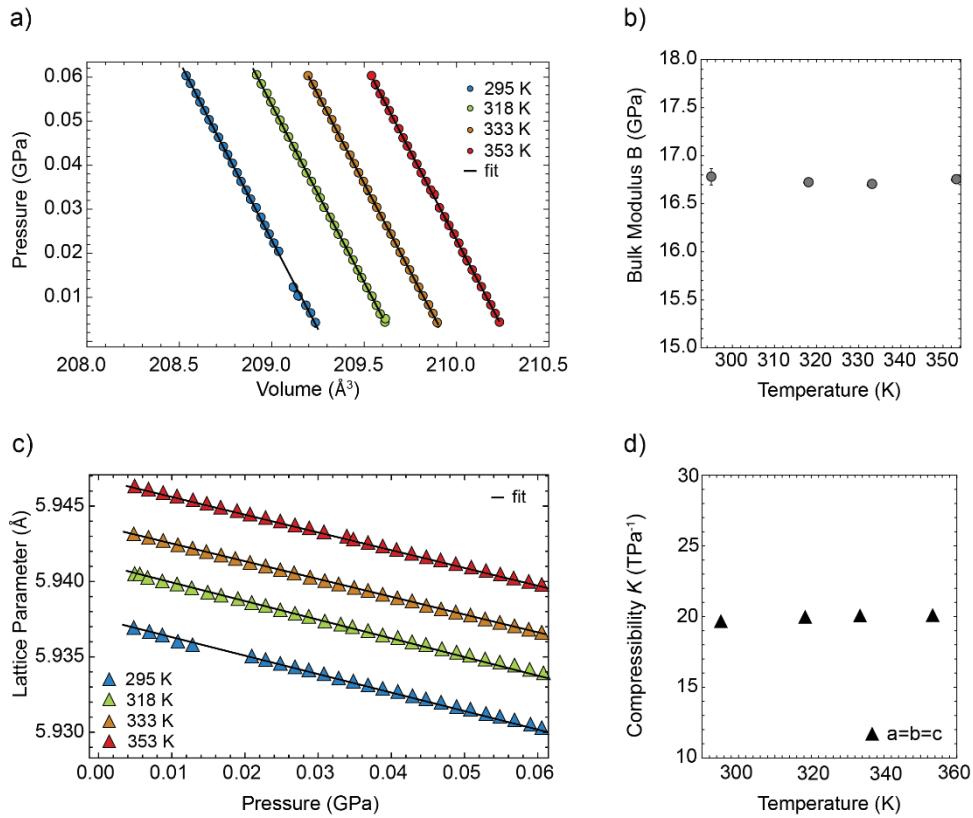


Figure S2. Unit-cell volume changes with pressure for MAPbBr₃ in the cubic Pm-3m phase and the corresponding fit to equation 1 of the main text. **b)** Bulk moduli obtained from the data shown in (a) and reported as a function of temperature in the cubic phase show no temperature dependence. **c)** Pressure-dependent lattice parameters of cubic MAPbBr₃ (Pm-3m space group) collected at 295, 318, 333, and 353 K obtained from refinements of synchrotron XRD pattern using the Rietveld method. **d)** Compressibility K of the lattice parameters in the cubic phase. Given the cubic structure, the compressibility is equal along all three axes.

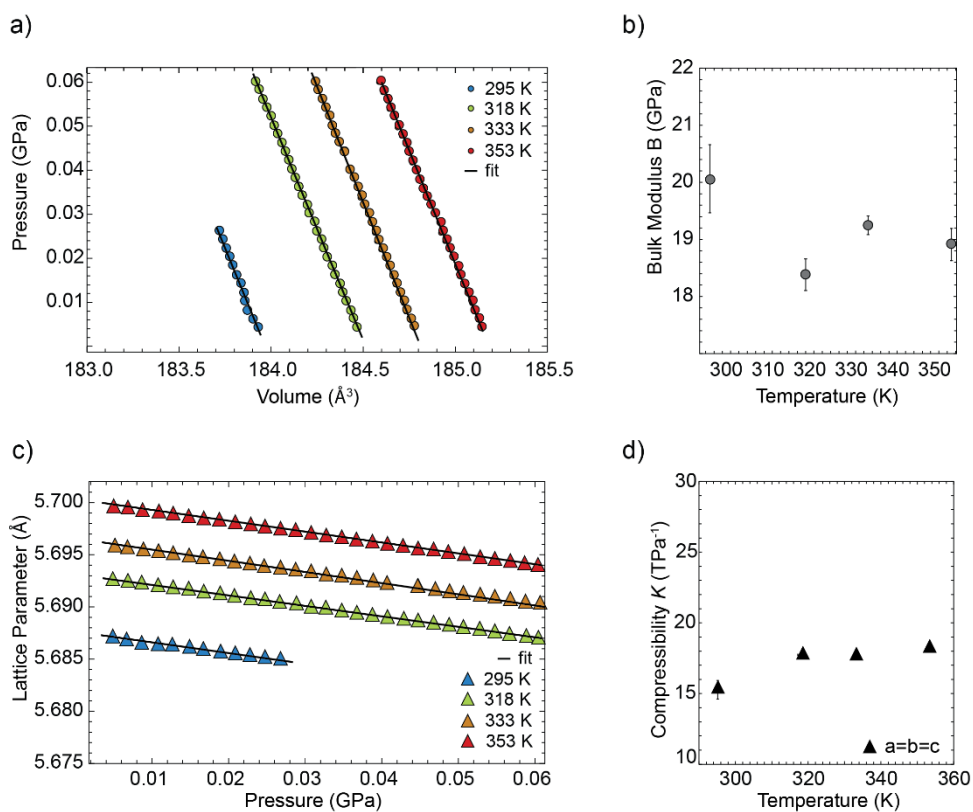


Figure S3. Unit-cell volume changes with pressure for MAPbCl₃ in the cubic Pm-3m phase and the corresponding fit to equation 1 of the main text. **b)** Bulk moduli obtained from the data shown in (a) and reported as a function of temperature in the cubic phase show no temperature dependence. **c)** Pressure-dependent lattice parameters of cubic MAPbCl₃ (Pm-3m space group) collected at 295, 318, 333, and 353 K obtained from refinements of synchrotron XRD pattern using the Rietveld method. **d)** Compressibility K of the lattice parameters in the cubic phase. Given the cubic structure, the compressibility is equal along all three axes.

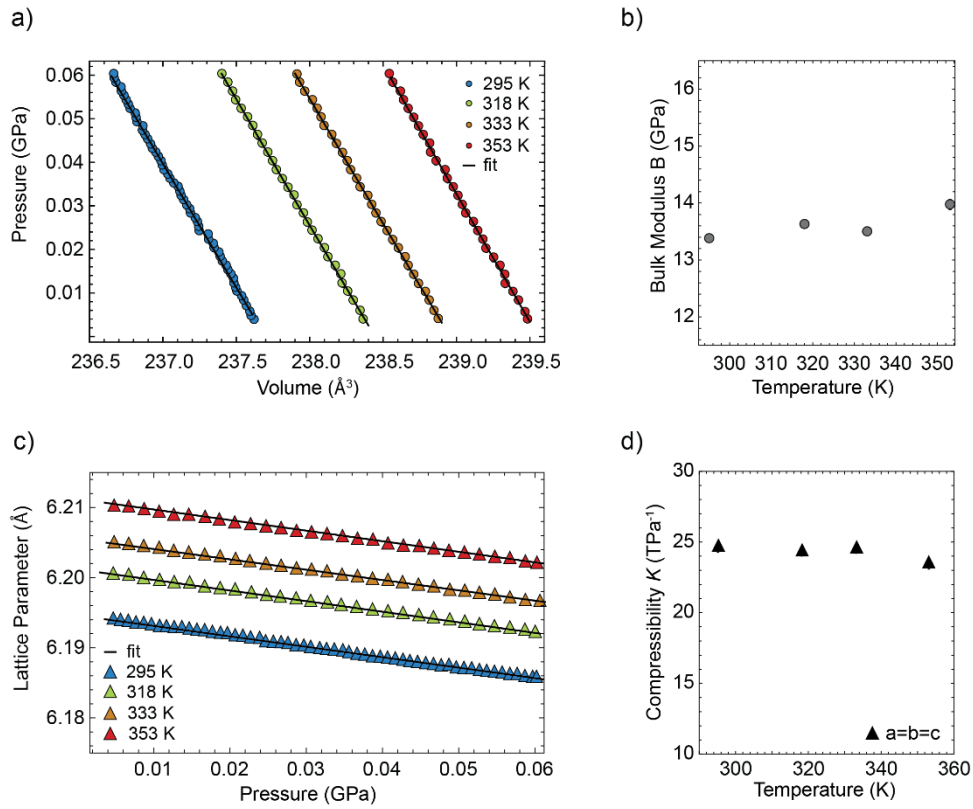


Figure S4. Unit-cell volume changes with pressure for MAPb(Br_{0.3}I_{0.7})₃ in the cubic Pm-3m phase and the corresponding fit to equation 1 of the main text. **b)** Bulk moduli obtained from the data shown in (a) and reported as a function of temperature in the cubic phase show no temperature dependence. **c)** Pressure-dependent lattice parameters of cubic MAPb(Br_{0.3}I_{0.7})₃ (Pm-3m space group) collected at 295, 318, 333, and 353 K obtained from refinements of synchrotron XRD pattern using the Rietveld method. **d)** Compressibility K of the lattice parameters in the cubic phase. Given the cubic structure, the compressibility is equal along all three axes.

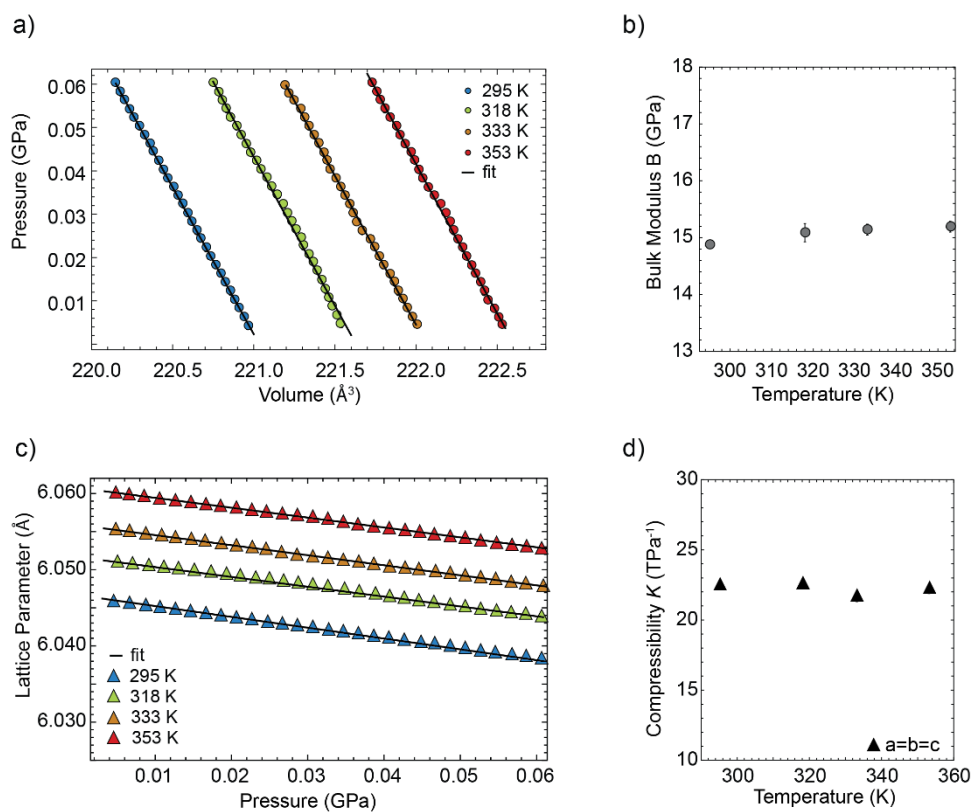


Figure S5. Unit-cell volume changes with pressure for MAPb(Br_{0.7}I_{0.3})₃ in the cubic Pm-3m phase and the corresponding fit to equation 1 of the main text. **b)** Bulk moduli obtained from the data shown in (a) and reported as a function of temperature in the cubic phase show no temperature dependence. **c)** Pressure-dependent lattice parameters of cubic MAPb(Br_{0.7}I_{0.3})₃ (Pm-3m space group) collected at 295, 318, 333, and 353 K obtained from refinements of synchrotron XRD pattern using the Rietveld method. **d)** Compressibility K of the lattice parameters in the cubic phase. Given the cubic structure, the compressibility is equal along all three axes.

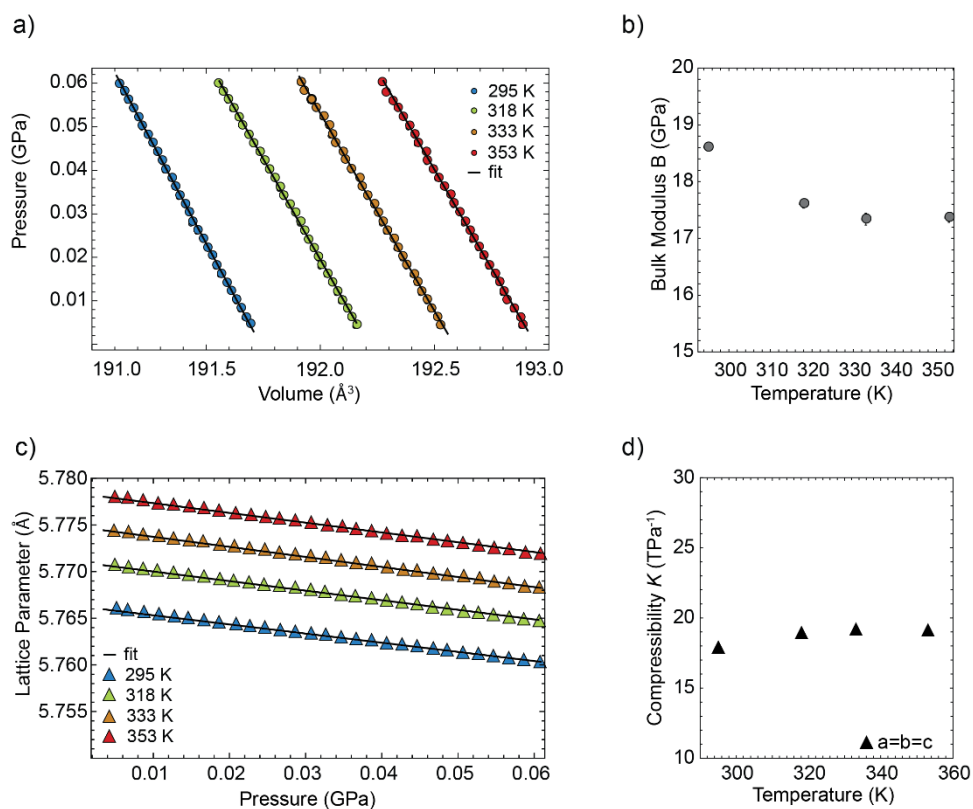


Figure S6. Unit-cell volume changes with pressure for MAPb(Br_{0.3}Cl_{0.7})₃ in the cubic Pm-3m phase and the corresponding fit to equation 1 of the main text. **b)** Bulk moduli obtained from the data shown in (a) and reported as a function of temperature in the cubic phase show no temperature dependence. **c)** Pressure-dependent lattice parameters of cubic MAPb(Br_{0.3}Cl_{0.7})₃ (Pm-3m space group) collected at 295, 318, 333, and 353 K obtained from refinements of synchrotron XRD pattern using the Rietveld method. **d)** Compressibility K of the lattice parameters in the cubic phase. Given the cubic structure, the compressibility is equal along all three axes.

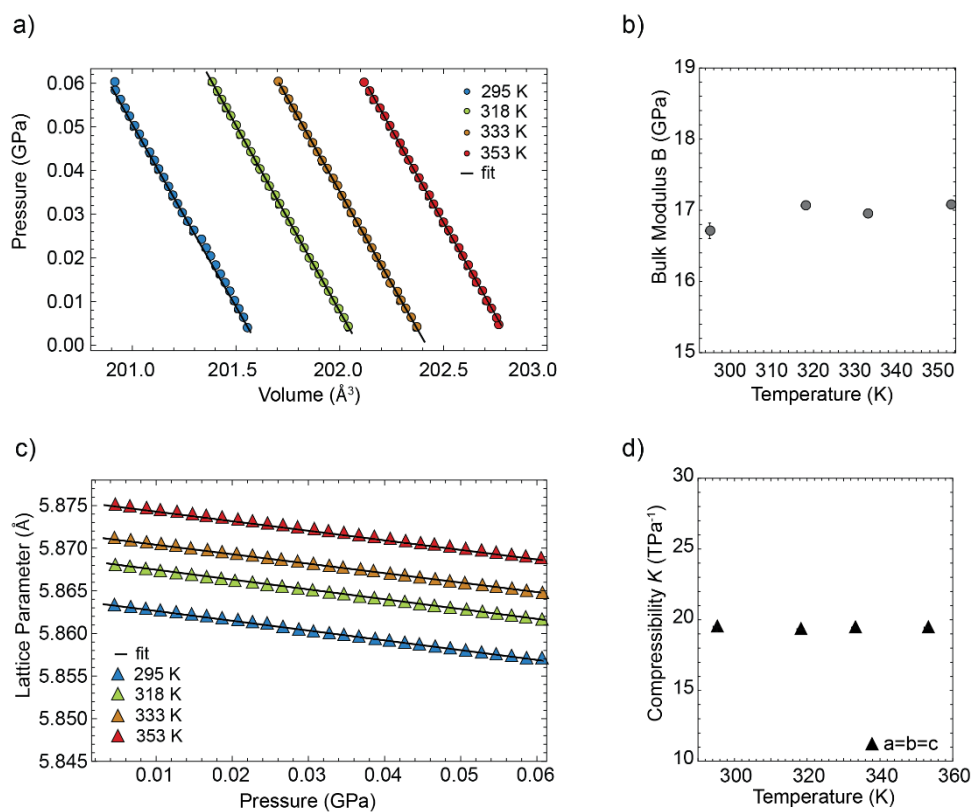


Figure S7. Unit-cell volume changes with pressure for MAPb(Br_{0.7}Cl_{0.3})₃ in the cubic Pm-3m phase and the corresponding fit to equation 1 of the main text. **b)** Bulk moduli obtained from the data shown in (a) and reported as a function of temperature in the cubic phase show no temperature dependence. **c)** Pressure-dependent lattice parameters of cubic MAPb(Br_{0.7}Cl_{0.3})₃ (Pm-3m space group) collected at 295, 318, 333, and 353 K obtained from refinements of synchrotron XRD pattern using the Rietveld method. **d)** Compressibility K of the lattice parameters in the cubic phase. Given the cubic structure, the compressibility is equal along all three axes.

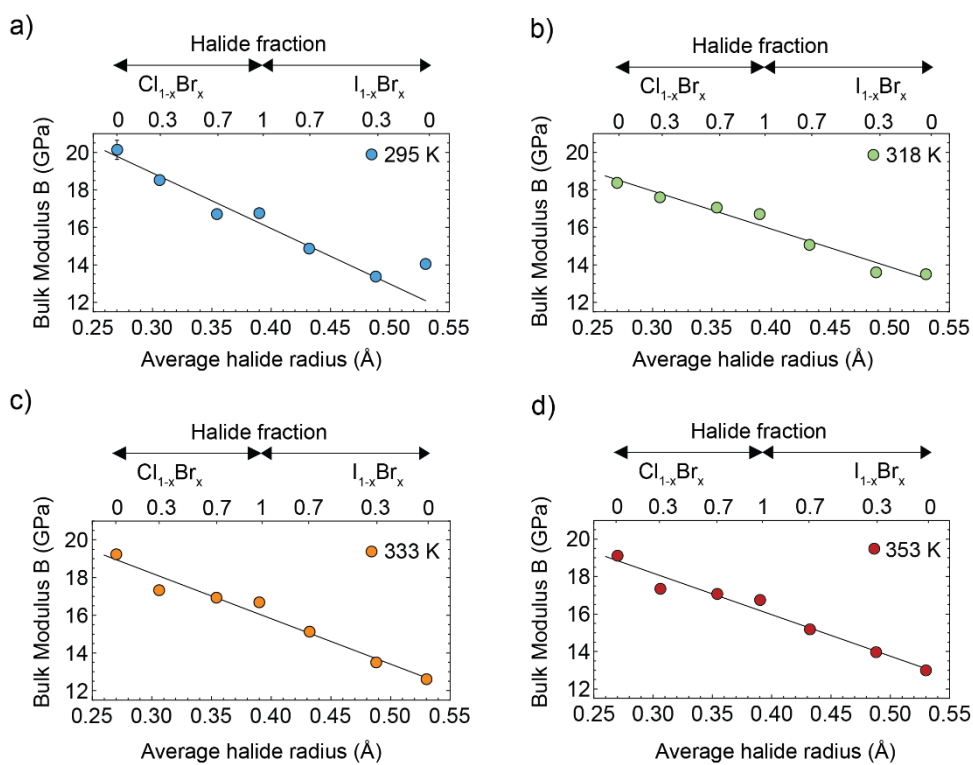


Figure S8. Linear fit of the bulk modulus as a function of the average halide radius at **a)** 295 K, **b)** 318 K, **c)** 333 K and **d)** 353K for single halide and mixed-halide compositions. Bulk moduli of compositions with intermediate average halide radius can be calculated using $B = 25.9 - 24.1x$ at room temperature, $B = 24 - 20.2x$ at 318K, $B = 25.4 - 24.1x$ at 333K, $B = 24.8 - 22.1x$ at 353K, where B is the bulk modulus and x the average halide radius.

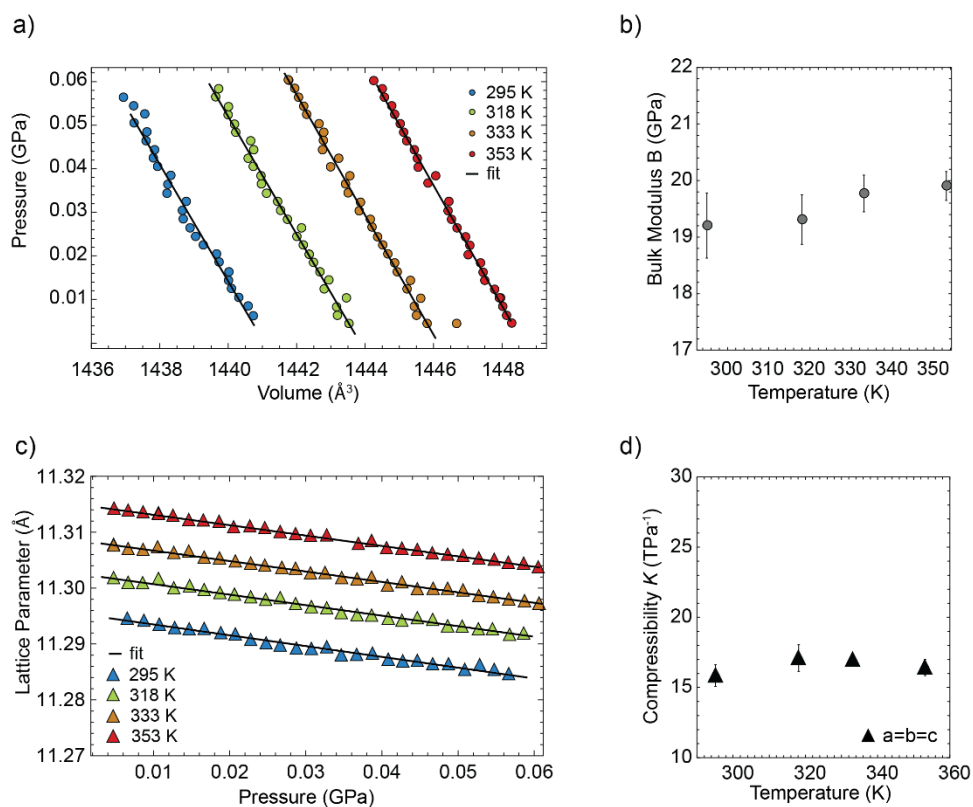


Figure S9. Unit-cell volume changes with pressure for $\text{Cs}_2\text{AgBiBr}_6$ in the cubic Fm-3m phase and the corresponding fit to equation 1 of the main text. **b)** Bulk moduli obtained from the data shown in (a) and reported as a function of temperature in the cubic phase show no temperature dependence. **c)** Pressure-dependent lattice parameters of cubic $\text{Cs}_2\text{AgBiBr}_6$ (Fm-3m space group) collected at 295, 318, 333, and 353 K obtained from refinements of synchrotron XRD pattern using the Rietveld method. **d)** Compressibility K of the lattice parameters in the cubic phase. Given the cubic structure, the compressibility is equal along all three axes.

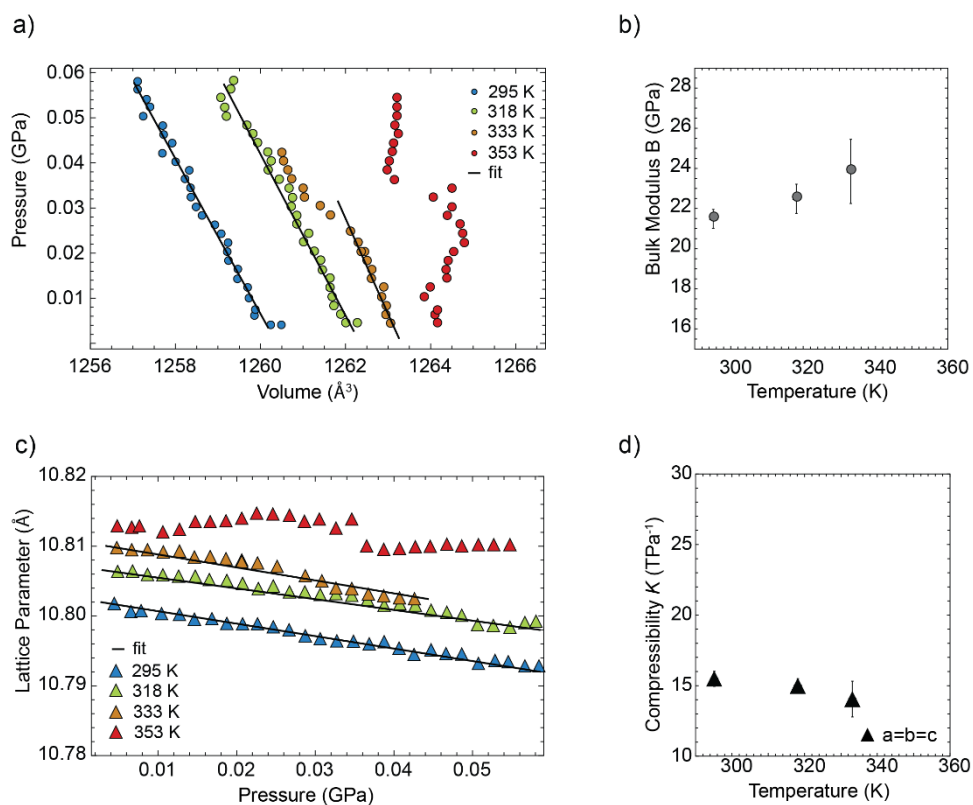


Figure S10. Unit-cell volume changes with pressure for $\text{Cs}_2\text{AgBiCl}_6$ in the cubic Fm-3m phase and the corresponding fit to equation 1 of the main text. **b)** Bulk moduli obtained from the data shown in (a) and reported as a function of temperature in the cubic phase show no temperature dependence. Due to the deviation in the linearity of P-V curve, we only fit the first half of the curve at 333 K, whereas we are not able to fit the P-V curve at 353 K. **c)** Pressure-dependent lattice parameters of cubic $\text{Cs}_2\text{AgBiCl}_6$ (Fm-3m space group) collected at 295, 318, 333, and 353 K obtained from refinements of synchrotron XRD pattern using the Rietveld method. **d)** Compressibility K of the lattice parameters in the cubic phase. Given the cubic structure, the compressibility is equal along all the three axes. Due to the deviation in the linearity of P-V curve at 353 K we do not report the corresponding compressibility.

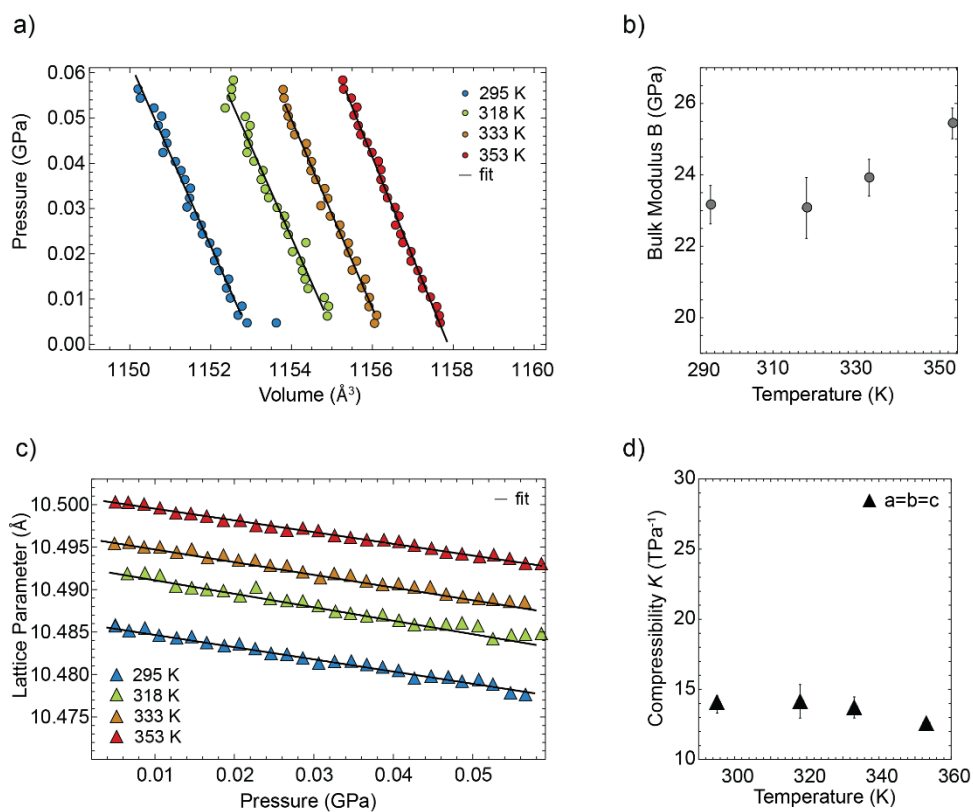


Figure S11. Unit-cell volume changes with pressure for $\text{Cs}_2\text{AgInCl}_6$ in the cubic Fm-3m phase and the corresponding fit to equation 1 of the main text. **b)** Bulk moduli obtained from the data shown in (a) and reported as a function of temperature in the cubic phase show no temperature dependence. **c)** Pressure-dependent lattice parameters of cubic $\text{Cs}_2\text{AgInCl}_6$ (Fm-3m space group) collected at 295, 318, 333, and 353 K obtained from refinements of synchrotron XRD pattern using the Rietveld method. **d)** Compressibility K of the lattice parameters in the cubic phase. Given the cubic structure, the compressibility is equal along all three axes.

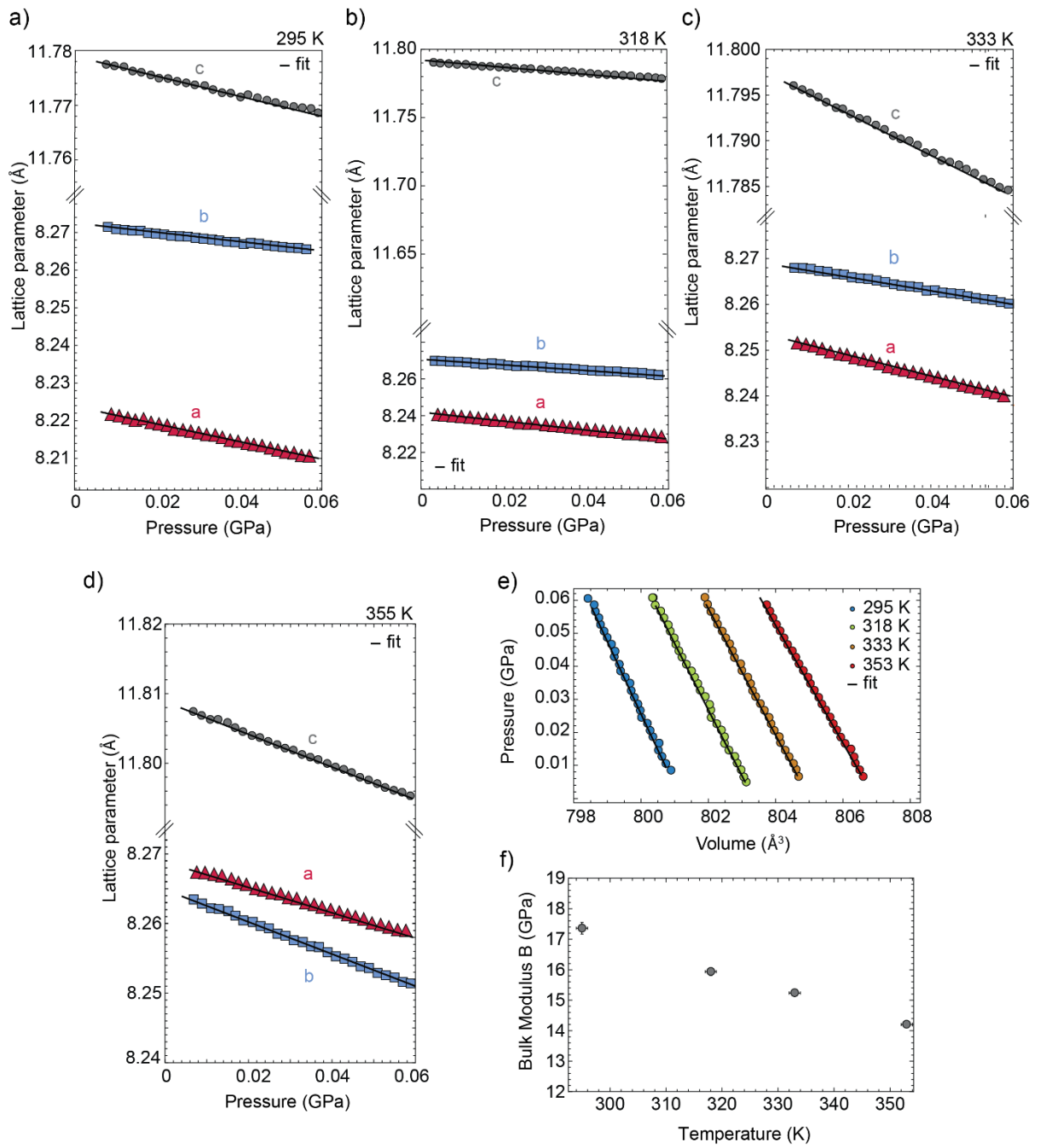


Figure S12. Pressure-dependent lattice parameters of the orthorhombic CsPbBr₃ (Pbnm space group) obtained from refinements of synchrotron XRD pattern at **a)** 295 K, **b)** 318 K, **c)** 333 K and **d)** 355 K using the Rietveld method. At 355 K, the lattice parameter *a* swap with that of *b*. **e)** Unit-cell volume changes with pressure for CsPbBr₃ in the orthorhombic Pbnm phase. **f)** Bulk modulus of CsPbBr₃ as a function of temperature obtained from the fit of the volume changes with pressure to equation 1 of the main text. Compressibility *K* is shown in **Figure 3b** in the main text.

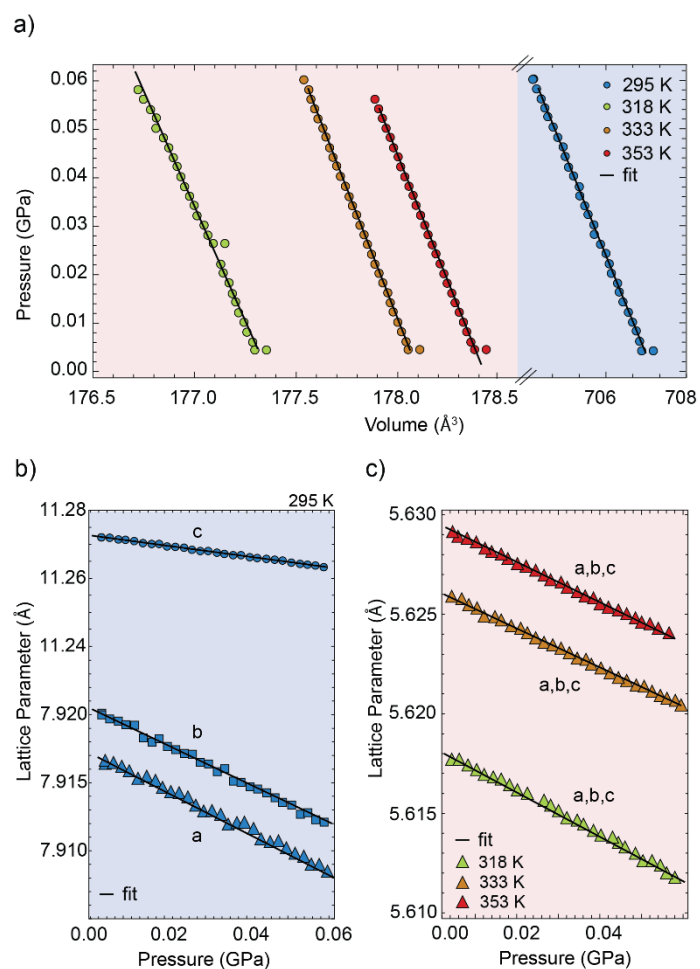


Figure S13. **a)** Unit-cell volume changes with pressure for CsPbCl₃ in the cubic Pm-3m phase (highlighted in red) and in the orthorhombic Pbnm phase (highlighted in blue) and the corresponding fit to equation 1 of the main text. **b)** Pressure-dependent lattice parameters of the orthorhombic CsPbCl₃ (Pbnm space group) collected at 295 K and **c)** of cubic Pm-3m phase at 318, 333, and 353 K obtained from refinements of synchrotron XRD pattern using the Rietveld method. Compressibility K is shown in **Figure 3b** in the main text.

Supporting Note 1. Fit for determining the bulk modulus as a function of temperature

For all the elpasolite, single halide (iodide, bromide, chloride) and mixed-halide perovskite series $\text{MAPb}(\text{Cl}_{1-x}\text{Br}_x)_3$ and $\text{MAPb}(\text{I}_{1-x}\text{Br}_x)_3$, we estimate the bulk moduli (B) by fitting the following function to the pressure-volume trends (**Figure 1c–d** and **Figure S1–S7**) at 295, 318, 333 and 353K.

$$B = -\frac{\Delta P}{\Delta V}V \quad (2)$$

with $\Delta P/\Delta V$ the partial derivative of pressure with respect to volume, and V the volume at ambient pressure. The results are reported below in **Table S1**.

	B (GPa) at 295 K	B (GPa) at 318 K	B (GPa) at 333 K	B (GPa) at 353 K
MAPbI₃	14.22	13.67	12.77	13.15
MAPbBr₃	16.94	16.87	16.85	16.91
MAPbCl₃	20.09	18.78	19.07	18.58
MAPb(Br_{0.3}I_{0.7})₃	13.53	13.78	13.66	14.13
MAPb(Br_{0.7}I_{0.3})₃	15.03	15.25	15.30	15.36
MAPb(Br_{0.3}Cl_{0.7})₃	18.77	17.77	17.50	17.53
MAPb(Br_{0.7}Cl_{0.3})₃	16.87	17.22	17.11	17.24
CsPbBr₃	17.53	16.10	15.40	14.36
CsPbCl₃	19.07	16.82	19.16	18.79
Cs₂AgBiBr₆	19.35	19.46	19.93	20.06
Cs₂AgBiCl₆	21.63	22.65	15.92	-
Cs₂AgInCl₆	23.31	23.23	24.07	25.59

Table S1. Bulk moduli, B , as a function of temperature for all compositions at 295 K, 318 K, 333 K, and 353 K.

Supporting Note 2. Axes-dependent and volumetric compressibility as a function of temperature

Considering that the elastic properties of non-cubic perovskites, such as tetragonal MAPbI₃, are in general anisotropic and therefore depend on crystallographic direction, we derived the compressibility of the specific crystal axes by monitoring their compression as a function of applied pressure (*e.g.*, for the compressibility along a-axis):

$$K_a = -\frac{(a_f - a_0)}{a_f} P \quad (3)$$

with a the lattice parameter, and $a_f - a_0$ the change in lattice parameter between the lattice parameter at the final (a_f) and initial (a_0) pressure. Similarly, the compressibility for b - and c -axis, for non-cubic perovskites, can be determined. The results are reported in **Table S2-S4**. The volume compressibility, K_V , i.e., the susceptibility of a material to compress upon external applied pressure, is inversely proportional to B . K_V is given by

$$K_V = K_a + K_b + K_c \quad (4)$$

i.e., K_V is the sum of the compressibility along each axis. Results are reported in **Table S5**.

	K_x (TPa ⁻¹) at 295 K		K_x (TPa ⁻¹) at 318 K		K_x (TPa ⁻¹) at 333 K		K_x (TPa ⁻¹) at 353 K	
CsPbBr₃	a	27.75	a	27.65	a	27.91	a	21.52
	b	13.89	b	17.01	b	18.71	b	28.61
	c	15.77	c	17.81	c	18.68	c	19.92
CsPbCl₃	a	19.21						
	b	19.12	-		-		-	
	c	14.49						

Table S2. Compressibility along the a, b, and c-axis, K_x (*with* $x = a, b, c$), for the orthorhombic compositions at 295 K, 318 K, 333 K, and 353 K.

	K_x (TPa ⁻¹) at 295 K		K_x (TPa ⁻¹) at 318 K		K_x (TPa ⁻¹) at 333 K	K_x (TPa ⁻¹) at 353 K
MAPbI₃	$a = b$	28.38	$a = b$	28.98	-	-
	c	13.93	c	15.64		

Table S3. Compressibility along the a, b, and c-axis, K_x (with $x = ab, c$), for the tetragonal compositions at 295 K, 318 K, 333 K, and 353 K.

	K_a (TPa ⁻¹) at 295 K	K_a (TPa ⁻¹) at 318 K	K_a (TPa ⁻¹) at 333 K	K_a (TPa ⁻¹) at 353 K
MAPbI₃	-	-	26.24	25.48
MAPbBr₃	19.73	19.84	19.83	19.80
MAPbCl₃	12.07	17.82	17.55	18.01
MAPb(Br_{0.3}I_{0.7})₃	24.75	24.26	24.54	23.70
MAPb(Br_{0.7}I_{0.3})₃	22.29	21.96	21.89	21.81
MAPb(Br_{0.3}Cl_{0.7})₃	17.84	18.83	19.13	19.09
MAPb(Br_{0.7}Cl_{0.3})₃	19.84	19.44	19.56	19.39
CsPbCl₃	-	17.76	17.49	17.95
Cs₂AgBiBr₆	17.29	17.19	16.79	16.68
Cs₂AgBiCl₆	15.46	14.77	21.02	16.00
Cs₂AgInCl₆	14.34	14.40	13.89	13.06

Table S4. Compressibility along the a-axis, K_a , for the cubic compositions at 295 K, 318 K, 333 K, and 353 K.

K_V (TPa ⁻¹)	K_V (TPa ⁻¹)	K_V (TPa ⁻¹)	K_V (TPa ⁻¹)
----------------------------	----------------------------	----------------------------	----------------------------

	at 295 K	at 318 K	at 333 K	at 353 K
MAPbI₃	70.69	73.60	78.72	76.44
MAPbBr₃	59.19	59.52	59.49	59.40
MAPbCl₃	36.21	53.46	52.65	54.03
MAPb(Br_{0.3}I_{0.7})₃	74.25	72.78	73.62	71.10
MAPb(Br_{0.7}I_{0.3})₃	66.87	65.88	65.67	65.43
MAPb(Br_{0.3}Cl_{0.7})₃	53.52	56.49	57.39	57.27
MAPb(Br_{0.7}Cl_{0.3})₃	59.52	58.32	19.56	58.68
CsPbBr₃	57.5	62.47	65.3	70.05
CsPbCl₃	52.82	53.29	52.49	53.86
Cs₂AgBiBr₆	50.64	50.75	49.84	49.68
Cs₂AgBiCl₆	45.69	43.00	60.18	-
Cs₂AgInCl₆	42.38	41.68	41.11	38.81

Table S5. Volumetric compressibility K_V for the compositions studied at 295 K, 318 K, 333 K, and 353 K.

Supporting Note 3. Calculation of the thermal expansivity

The thermal expansion coefficient, α_L , of a material is defined as the relative expansion in one dimension per unit of temperature:

$$\alpha_L = \frac{1}{L} \frac{\Delta L}{\Delta T} \quad (5)$$

For solids α_L is typically temperature-independent. So, we expect a linear dependence of the lattice parameters, $L = a, b$, and c , over our range of measured temperatures. As such for $L = a$:

$$\alpha_a = \frac{1}{a} \frac{\Delta a}{\Delta T} \quad (6)$$

Rewriting eq. (6) provides:

$$\frac{\Delta a}{a} = \alpha_a \Delta T \quad (7)$$

For an α_a that is independent to temperature this yields:

$$a(T) = a_0 + \alpha_a a_0 T \quad (8)$$

where a_0 is the lattice parameter extrapolated to $T = 0$ K. For some compositions we observe non-linear expansion along certain crystal axes. In this case a single value for α_a does not suffice and integration of eq. (6) over the experimental temperature range is required:

$$a(T) = a_0 \text{Exp} \left[\int_{T_1}^{T_2} \alpha_a(T) dT \right] \quad (9)$$

with $a(T)$ a second order polynomial function ($a(T) = m_1 T^2 + m_2 T + a_0$) describing the lattice parameter as a function of temperature. Solving eq. (9) for α_a gives:

$$\alpha_a(T) = \frac{m_2 + 2m_1 T}{a_0 + T(m_2 + m_1 T)} \quad (10)$$

Table S6 provides the optimized parameters for eq. (10).

i)	Orthorhombic			
	Crystal axis	m_1	m_2	a_0
MAPbI ₃	$a (\times 10^{-5} \text{ K}^{-1})$	3.81		
	$b (\times 10^{-5} \text{ K}^{-1})$	2.02		
	$c (\times 10^{-5} \text{ K}^{-1})$	5.81		
MAPbBr ₃	$a (\times 10^{-5} \text{ K}^{-1})$	9.04		
	$b (\times 10^{-5} \text{ K}^{-1})$	-2.79		
	$c (\times 10^{-5} \text{ K}^{-1})$	1.00		
MAPbCl ₃	a	-8.45×10^{-7}	5.63×10^{-4}	11.15
	b	1.86×10^{-6}	-3.05×10^{-4}	11.36
	c	8.60×10^{-7}	-3.26×10^{-5}	11.28
CsPbBr ₃	$a (\times 10^{-5} \text{ K}^{-1})$	7.68		
	b	1.22×10^{-6}	-6.14×10^{-4}	8.34
	$c (\times 10^{-5} \text{ K}^{-1})$	3.51		
CsPbCl ₃	a	-9.82×10^{-7}	9.18×10^{-4}	7.72
	b	-4.61×10^{-7}	5.14×10^{-4}	11.14
	c	1.41	-5.80×10^{-4}	7.96

ii)	Tetragonal			
	Crystal axis	m_1	m_2	a_0
MAPbI ₃	$a = b$	1.03×10^{-6}	5.10×10^{-5}	8.76
	$c (\times 10^{-5} \text{ K}^{-1})$	0.34		
MAPbBr ₃	$a = b (\times 10^{-5} \text{ K}^{-1})$	6.99		
	c	-5.52×10^{-6}	1.63×10^{-3}	11.77

iii)	Cubic ($\times 10^{-5} \text{ K}^{-1}$)
------	---

MAPbI₃	4.04
MAPbBr₃	3.53
MAPbCl₃	3.51
CsPbBr₃	3.27**
CsPbCl₃	3.02
Cs₂AgBi(Br_{0.33}I_{0.67})₆	5.08**
Cs₂AgBiBr₆	2.86
Cs₂AgBiCl₆	2.42
Cs₂AgInCl₆	2.49
Cs₂Ag(Bi_{0.5}In_{0.5})Br₆	2.84**
Cs₂Ag(Bi_{0.5}Sb_{0.5})Br₆	3.34**
Cs₂Ag(Bi_{0.9}Fe_{0.1})Br₆	3.16**

Table S6. Optimized parameters to describe $\alpha(T)$ for a given temperature range.

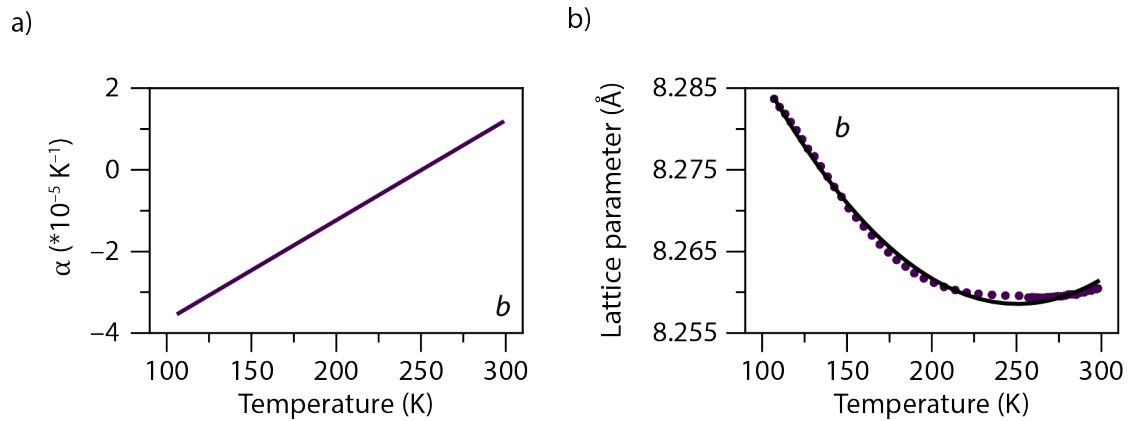


Figure S16. a) Non-linear α of the lattice parameter, b , of orthorhombic CsPbBr₃ between 100 and 300 K. The optimized parameters for this plot are provided in **Table S6 i)**. **b)** Temperature dependent lattice parameter of the lattice parameter, b , of orthorhombic CsPbBr₃ between 100 and 300 K (dots) and the polynomial fit (dotted line) to extract the temperature dependent α given in **a)**.

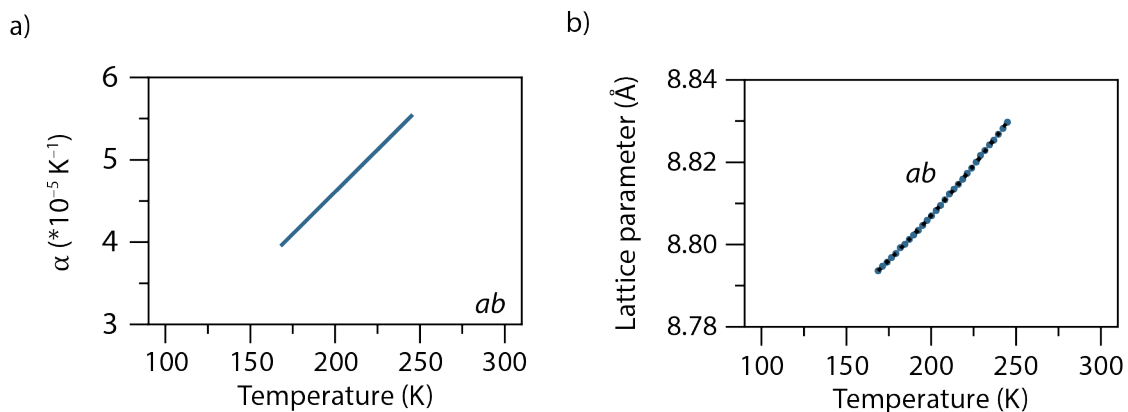


Figure S17. a) Non-linear α of the lattice parameter, ab , of tetragonal MAPbI₃ between 170 and 250 K. The optimized parameters for this plot are provided in **Table S6 ii**. **b)** Temperature dependent lattice parameter of the lattice parameter, ab , of tetragonal MAPbI₃ between 170 and 250 K (dots) and the polynomial fit (dotted line) to extract the temperature dependent α given in **a**).

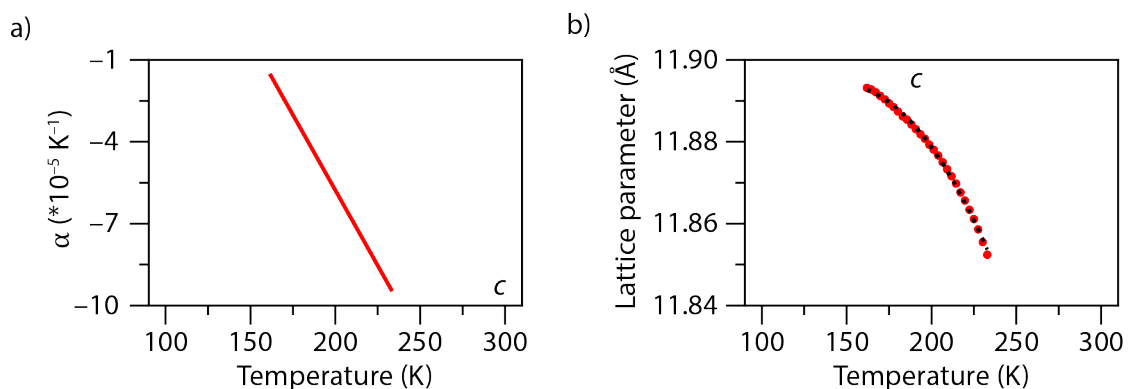


Figure S18. a) Non-linear α of the lattice parameter, c , of tetragonal MAPbBr₃ between 160 and 230 K. The optimized parameters for this plot are provided in **Table S6 ii**. **b)** Temperature dependent lattice parameter of the lattice parameter, c , of tetragonal MAPbBr₃ between 160 and 230 K (dots) and the polynomial fit (dotted line) to extract the temperature dependent α given in **a**).

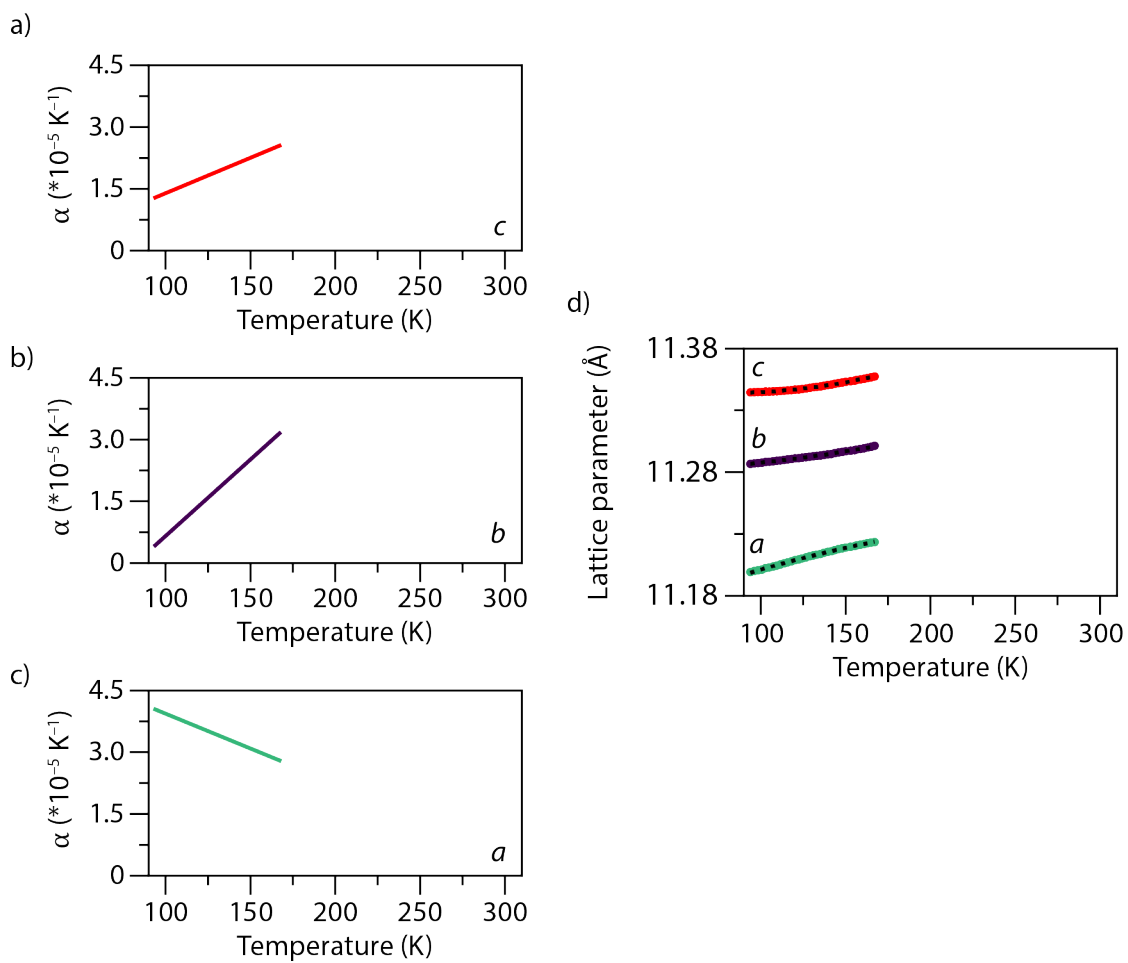


Figure S19. a–c) Non-linear α of the lattice parameters, *abc*, of orthorhombic MAPbCl₃ between 100 and 170 K. The optimized parameters for this plot are provided in **Table S6 i)**. **d)** Temperature dependent lattice parameter of the lattice parameter, *abc*, of orthorhombic MAPbCl₃ between 100 and 170 K (dots) and the polynomial fits (dotted line) to extract the temperature dependent α given in **a–c)**.

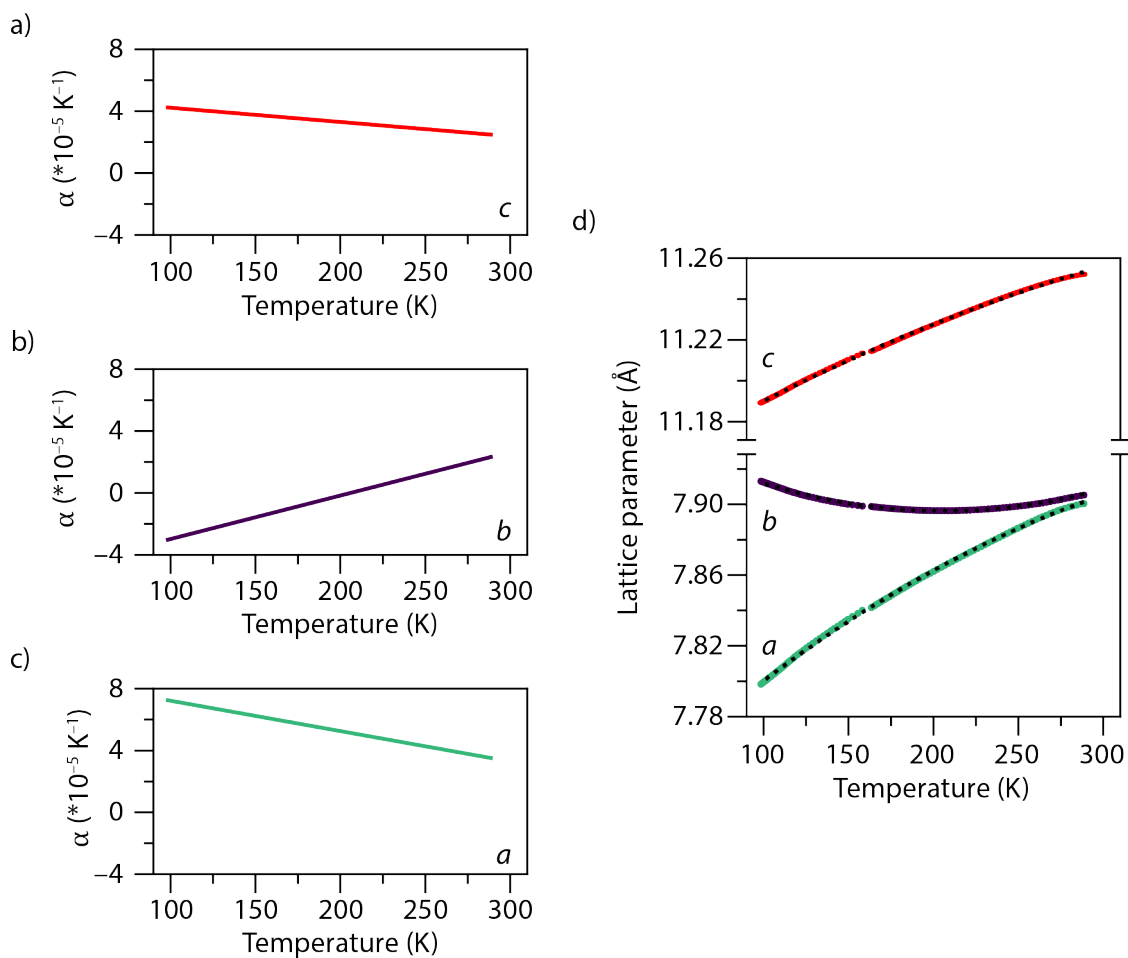


Figure S20. a–c) Non-linear α of the lattice parameters, *abc*, of orthorhombic CsPbCl₃ between 100 and 300 K. The optimized parameters for this plot are provided in **Table S6 i**). **d)** Temperature dependent lattice parameter of the lattice parameter, *abc*, of orthorhombic CsPbCl₃ between 100 and 300 K (dots) and the polynomial fits (dotted line) to extract the temperature dependent α given in **a–c**).

Supporting Note 4. Lab-based temperature dependent X-ray diffraction

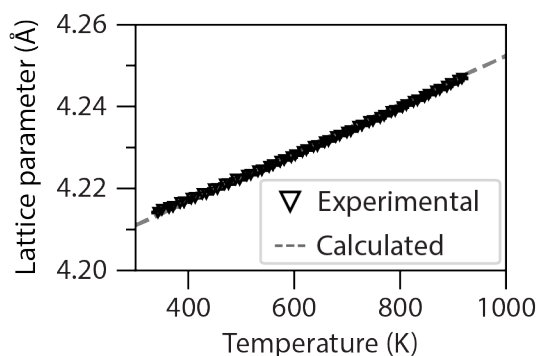
First the temperature inside the cell was calibrated by measuring the lattice expansion of MgO over a temperature range of 300 K to 900 K. From literature the lattice parameter as a function of temperature is given by⁵:

$$a(T) = 4.2094 + 5.92 \times 10^{-5} \times T \quad (1)$$

with T the temperature in degrees Celsius. The lattice parameter of MgO as a function of temperature was determined using the same refinement method as described in the main text (**Figure S14a**). The experimental temperature was scaled with a factor of 1.05 to match the α of MgO reported in the literature (eq. (1)). No correction was performed to adjust for the change in sample position as a consequence of the expanding sample holder upon increasing the temperature.

To verify the reproducibility of our experiments, the α of Cs₂AgBiBr₆ (**Figure S14**, blue data points) and CsPbBr₃ (**Figure S15**) was determined and compared to the results from our experiments using synchrotron radiation. The discrepancy observed for these values can be attributed when considering the different experimental setups and conditions, such as the (mono-chromatic) light source, less accurately defined sample position, used detector, atmosphere, etc. We, however, note that quality of the lab-based data is still sufficient to apply the same refinement method as described in the main text. As such, we determined the α of Cs₂Ag(Bi_{1-x}B_x)Br₆ with (B_x = In_{0.5}, Sb_{0.5} and Fe_{0.1}) and Cs₂AgBi(Br_{0.33}I_{0.67})₆ (**Figure S14b** and **Table 1**).

a)



b)

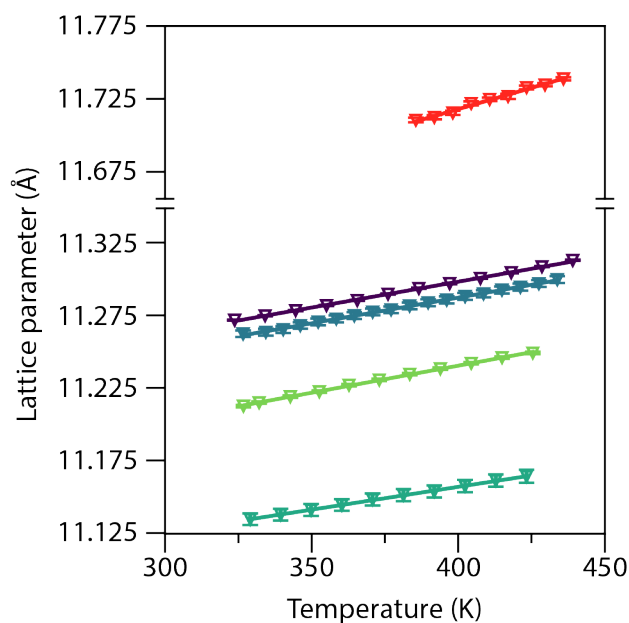


Figure S14. a) Temperature-dependent lattice parameter of MgO obtained using Rietveld refinement method of *in-situ* XRD patterns collected from 300 K to 900 K using a lab-based X-ray source. The dotted grey line represents eq. (1). **b)** Temperature-dependent lattice parameters of cubic alloyed elpasolites obtained using Rietveld refinement method of *in-situ* XRD patterns collected between 325 and 450 K using a lab-based X-ray source. From top to bottom the lines represent: Cs₂AgBi(Br_{0.3}I_{0.7})₆, Cs₂AgBiBr₆, Cs₂Ag(Bi_{0.9}Fe_{0.1})Br₆, Cs₂Ag(Bi_{0.5}Sb_{0.5})Br₆, and Cs₂A(Bi_{0.5}In_{0.5})Br₆.

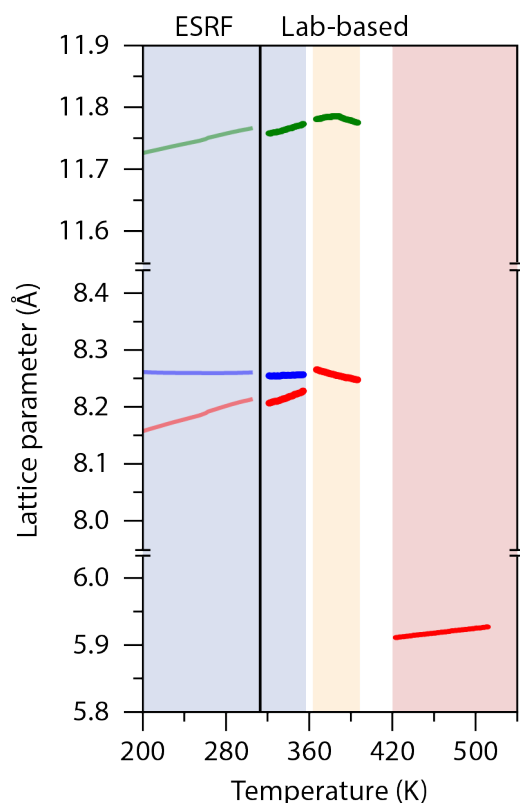


Figure S15. Lattice expansion of CsPbBr₃ over a temperature range of 200 to 540 K determined with synchrotron (<315 K) and lab-based X-ray sources (>315 K). For cubic CsPbBr₃ (>420 K) the α was determined see **Table 1** in the main text.

References

- (1) Dyadkin, V.; Pattison, P.; Dmitriev, V.; Chernyshov, D. A New Multipurpose Diffractometer PILATUS@SNBL. *J. Synchrotron Rad.* **2016**, *23*, 825–829.
- (2) C. J. McMonagle; Allan, D. R.; Warren, M. R.; Kamenev, K. V.; Turner, G. F.; Moggach, S. A. High-Pressure Sapphire Capillary Cell for Synchrotron Single-Crystal X-Ray Diffraction Measurements to 1500 Bar. *J. Appl. Cryst.* **2020**, *53*, 1519–1523.
- (3) J. Cosier; Glazer, A. M. A Nitrogen-Gas-Stream Cryostat for General X-Ray Diffraction Studies. *J. Appl. Crystallogr.* **1986**, *19*, 105–107.
- (4) Marshall, K.; Emerich, H.; McMonagle, C.; Fuller, C.; Dyadkin, V.; Chernyshov, D.; van Beek, W. A New High Temperature, High Heating Rate, Low Axial Gradient Capillary Heater. *J. Synchrotron Radiat.* **2023**, *30*, 267–272.
- (5) Swanson, D. K.; Prewitt, C. T. A New Radiative Single-Crystal Diffractometer Microfurnace Incorporating MgO as a High-Temperature Cement and Internal Temperature Calibrant. *J. Appl. Cryst.* **1986**, *19*, 1–6.